Chemical Engineering Journal 522 (2025) 167518

Contents lists available at ScienceDirect

Chemical Engineering Journal

journal homepage: www.elsevier.com/locate/cej

Adaptive bioinspired Light Emitting Diode-Internet of Things (LED-IoT) assisted solar packed bed photocatalytic reactor system for naproxen removal from real wastewater matrices☆

Adam Kubiak [a,*], Serena Lima [b], Gianluca Li Puma [b,*]

[a] Faculty of Chemistry, Adam Mickiewicz University, Poznan, Poland
[b] Environmental Nanocatalysis & Photoreaction Engineering, Department of Engineering, University of Palermo (UNIPA), Palermo, Italy

ARTICLE INFO

Keywords:
TiO_2-based photocatalyst
Biomimetic approach
IoT-controlled system
Flow-through photoreactor
Complex aqueous environments

ABSTRACT

This study investigates a novel solar-driven photocatalytic system integrating real time Internet of Things (IoT) controlled adaptive lighting with bioinspired TiO_2-based photocatalysts immobilized on natural 3D scaffold materials (*Luffa cylindrica* and marine sponge) for the degradation of a model pharmaceutical (naproxen) in real wastewater matrices. The system integrates a five-stage flow-through packed-bed reactor with adaptive LED activation, autonomously regulated via light sensors to compensate for fluctuating solar irradiance. Field tests conducted in Palermo (Italy) and Poznan (Poland) demonstrated consistent photocatalytic performance with less than 11 % variation in naproxen degradation efficiency despite significantly different solar irradiation conditions. The results highlight the superior durability and activity of the *Luffa cylindrica* over the marine sponge photocatalyst and validate the robustness of IoT-controlled hybrid lighting under real environmental matrices (tap water, municipal wastewater, and hospital sewage). This work introduces a scalable and resilient approach for solar-assisted pharmaceutical removal, with strong potential for integration into wastewater treatment infrastructures located in diverse climatic regions.

1. Introduction

Pharmaceuticals residues in water constitute a major class of contaminants of emerging concern having a significant impact on the aquatic environment including surface water, groundwater, and drinking water [1]. These compounds primarily enter aquatic ecosystems through municipal and hospital wastewaters, through industrial discharge, aquaculture, animal farming and through the improper disposal of medications [2]. Due to their persistence, pharmaceuticals can cause long-term ecotoxicological effects, including endocrine disruption, immune impairment, and behavioural changes in aquatic organisms [3]. Pharmaceuticals also contribute to the development of antimicrobial resistance (AMR), which is now recognized as a major global health threat [4]. In Europe, AMR accounts for approximately 25,000 deaths annually, with projections estimating 10 million deaths per year globally by 2050 if no action is taken [5]. Despite these risks, current regulations are insufficient, with no unified international standards governing pharmaceutical pollution in wastewater [6]. Current wastewater treatment plants (WWTPs), while effective for organic matter removal, lack the infrastructure to efficiently eliminate pharmaceutical residues, resulting in their continuous release into aquatic environments at concentrations ranging from nanograms to micrograms per liter [7].

Non-steroidal anti-inflammatory drugs (NSAIDs), such as ibuprofen, diclofenac, ketoprofen, and naproxen (NPX), are a class of pharmaceuticals frequently detected in wastewater [8]. Studies have reported ibuprofen concentrations ranging from 0.5 to 37 μg L^{-1} in influents and 0.04 to 19.09 μg L^{-1} in effluents of WWTPs, while NPX and diclofenac concentrations in the effluent of municipal wastewater have been observed at levels up to 9.6 μg L^{-1} [9] and 2.3 μg L^{-1} [10] respectively. These findings highlight the widespread occurrence of NSAIDs in wastewater and the limitations of current treatment methods in their degradation.

Given these limitations, alternative approaches such as advanced oxidation processes (AOPs) have gained attention, with photocatalysis emerging as a promising sustainable method due to its ability to degrade

☆ This article is part of a Special issue entitled: 'Dion Dionysiou Memorial Issue' published in Chemical Engineering Journal.

* Corresponding authors.
E-mail addresses: adam.kubiak@amu.edu.pl (A. Kubiak), gianluca.lipuma@unipa.it (G. Li Puma).

https://doi.org/10.1016/j.cej.2025.167518
Received 2 June 2025; Received in revised form 9 August 2025; Accepted 20 August 2025
Available online 21 August 2025

and mineralize pharmaceutical residues in water through the in-situ generation of reactive oxygen species (ROS), without the need of chemical additives and also using solar light. However, despite its advantages, its practical implementation is constrained by engineering challenges related to reactor design, scalability, light distribution, operational stability and catalyst activity [11]. Among these, a key issue affecting reactor design is the inefficient distribution of light in the reactor, which ultimately limits the overall removal of pharmaceutical residues from water. Common reactor geometries, such as annular and flat-bed designs, may suffer from non-uniform distribution of the photon flux, meaning that only a fraction of the catalyst surface is effectively illuminated, while regions of the reactor away from the light sources remain underutilized [12]. This limitation is particularly problematic for TiO_2-photocatalysis systems, where photon absorption occurs primarily near the reactor front window, reducing the efficiency in bulk water systems. Additionally, the lack of standardized reactor designs has hindered the industrial deployment of photocatalysis, as no single configuration has demonstrated universal efficiency for large-scale applications [13]. Beyond reactor design, solar-driven photocatalysis is highly dependent on sunlight availability, with efficiency varying with atmospheric conditions, seasonal variations and geographical location. Studies show that solar irradiance in Northern Europe during winter can be 5–10 times lower than in Southern Europe, drastically affecting system performance [14]. Cloud cover and seasonal changes further reduce photocatalytic activity, making sunlight-dependent systems unreliable as a standalone treatment [15]. One approach to mitigate these limitations concerns the use of solar concentrators, which enhance the light intensity reaching the photocatalyst surface. However, while these systems improve the photon flux reaching the reactor, they do not fully compensate for prolonged periods of low sunlight exposure, such as during overcast days or in winter months or at night [16]. Furthermore, many large-scale photocatalytic reactors continue to rely on suspended catalysts, which require post-treatment separation, increasing operational costs. Immobilized catalysts, while simplifying separation, often are limited by reacting species mass transfer and reduced active surface area, lowering the overall efficiency of the treatment system [17]. These engineering constraints continue to slow the integration of photocatalysis into full-scale wastewater treatment facilities, underscoring the need for innovative reactor designs that optimize light penetration, catalyst utilization, and process stability.

To address these challenges, this study introduces, for the first time, a flow-through solar tubular photocatalytic reactor that integrates real-time Internet of Things controlled adaptive lighting with bioinspired TiO_2-based photocatalysts immobilized on bionatural 3D scaffold materials. The system employs a five-stage packed reactors in series configuration and dynamically regulates the intensity of LED illumination located beneath the tubes based on sensor-detected fluctuations in natural sunlight to compensate for periodical reductions of the solar photon flux. This ensures consistent and continuous photocatalytic activity even under variable weather and seasonal conditions and at night. The use of sustainable biomatrices, *Luffa cylindrica* and marine sponge, as photocatalyst scaffolds enhances light penetration through the bed, mass transfer, and structural durability, offering significant advantages over conventional suspended or other immobilized photocatalyst systems. Together, these features mitigate the critical limitations of existing photocatalytic designs, demonstrating a scalable, low-energy, and field-tested solution for degradation of water contaminants and pharmaceutical residues under real-world conditions in complex wastewater matrices.

2. Materials and method

2.1. Materials

The materials used included titanium(IV) isopropoxide (TTIP, 97 %, Thermo Scientific), triethylamine (TEA, 99.5 %, Thermo Scientific), isopropanol (IPA, 99.5 %, Fisher Scientific), ammonia solution ($NH_3{\cdot}H_2O$, 25 %, Fisher Scientific), hexadecyltrimethylammonium bromide (≥98 % purity, CTAB, Merck), naproxen (NPX, analytical standard, Merck), and commercial sponges obtained from INTIB GmbH (Germany). All reagents were of analytical grade and were used without further purification. Deionized water with a resistivity of 18.2 MΩ•cm, produced using a Milli-Q water purification system (Merck Millipore, USA), was used as the solvent in all experimental procedures.

2.2. Synthesis of bioinspired TiO_2-based photocatalysts

The synthesis of the photocatalysts consisted of two main stages: the preparation of TiO_2 nanoparticles and the fabrication of the bioinspired materials. The synthesis of TiO_2 was carried out following the methodology described in our previous study [18]. In a typical synthesis, 1 L of isopropyl alcohol (IPA) and 40 mL of titanium tetraisopropoxide (TTIP) were introduced into an IKA Laboratory reactor equipped with an anchor stirrer (IKA Werke GmbH & Co, Germany). The mixture was stirred at a constant speed of 150 rpm for 30 min before the addition of 20 mL of triethanolamine (TEA) solution. Subsequently, 100 mL of 25 % ammonia solution was introduced at a constant rate of 5 mL min^{-1} using an ISM833A peristaltic pump (ISMATEC, Germany). The reaction mixture was continuously stirred at room temperature at 150 rpm for 24 h. Following the reaction, the resulting colloidal suspension was allowed to gel, and the precipitate was washed multiple times with deionized water and ethanol to remove residual impurities. The obtained powder was dried at 100 °C for 24 h and subsequently calcined at 300 °C for 2 h (with a heating rate of 2 °C min^{-1}) using a Nabertherm P320 Controller (Germany). The final TiO_2 material was used for the synthesis of bioinspired photocatalysts.

The preparation of the TiO_2-based bioinspired photocatalysts involved marine sponge and *Luffa cylindrica* frameworks. The natural scaffolds were initially cleaned and divided into small sections (3 × 2 cm each). These segments were immersed in a 0.5 wt% CTAB solution and stirred at room temperature for 30 min to enhance surface wettability. The pre-treated sponge pieces were then placed in a dispersion containing 500 mg of TiO_2 in 50 mL of deionized water. The mixture was transferred to a microwave reactor (Anton Paar Monowave 450, Austria) and heated at 60 °C for 30 min. After microwave treatment, the TiO_2-coated marine sponge and *Luffa cylindrica* materials were carefully removed using tweezers and air-dried for 48 h and stored in sealed containers for further characterization and photoactivity testing.

2.3. Material characterization

The photocatalysts were subjected to comprehensive physicochemical characterization both before and after the photocatalytic process. Structural and morphological analyses were performed using X-ray diffraction (XRD), scanning electron microscopy (SEM), high-resolution transmission electron microscopy (HR-TEM), and energy-dispersive X-ray spectroscopy (EDX). The surface chemistry and elemental composition of the materials were examined using X-ray photoelectron spectroscopy (XPS). Optical properties were investigated through diffuse reflectance spectroscopy (DRS) and fluorescence spectroscopy. Additionally, light distribution measurements, thermal imaging analysis, and LED light source spectral characterization were conducted to assess the efficiency and operational stability of the LED-driven photocatalytic system. Attenuated total reflectance Fourier-transform infrared spectroscopy (FTIR-ATR) was employed to evaluate potential surface modifications of the photocatalytic materials following the photocatalytic process. Detailed results of these analyses are provided in the Supplementary Information (SI).

2.4. Photocatalytic performance

2.4.1. Design of LED-IoT system

The photocatalytic flow-through tubular packed system consisted of several essential components arranged in a modular configuration, enabling in-series operation through multiple reactor units to enhance the contaminant degradation efficiency. At its core was an aluminium housing (171 × 121 × 51 mm) sourced from Transfer Multisort Elektronik (Poland), which functioned as a heat sink for the LEDs. The housing was modified by drilling parallel holes (13.5 mm in diameter) to accommodate borosilicate glass tubes filled with bioinspired TiO_2-based photocatalysts immobilized on *Luffa cylindrica* or marine sponge scaffolds. Each borosilicate tube (Conductance, Poland) featured an outer diameter of 13 mm and a wall thickness of 1.5 mm. The central 12 cm section of each tube was directly exposed to the LED light source and defined as the irradiated zone. To enable continuous and controlled flow between stages, the tubes were connected in series using 15 mm silicone hoses. The total mass of the catalyst-loaded tube (TiO_2 deposited on the biomimetic support) was determined gravimetrically by subtracting the known mass of an empty tube (~22.5 g). This value represents the combined mass of the TiO_2 photocatalyst and its supporting scaffold.

The individual photocatalyst masses for the marine sponge-based system ranged from 2.11 g to 2.72 g, with an average loading of 2.39 ± 0.20 g per tube. Given that the average mass of the biomimetic scaffold placed in the tube was 1.21 g, the average amount of deposited TiO_2 was approximately 1.18 g per tube. For the luffa-based system, the catalyst mass ranged from 1.86 g to 2.16 g, with an average of 2.01 ± 0.15 g. Considering that the average mass of the luffa scaffold was 1.12 g, the amount of TiO_2 was approximately 0.89 g per tube.

The recirculation system included a 500 mL glass tank and a submersible pump (Hsabo, China) with a maximum flow rate of 200 L h^{-1} and IPX8 protection rating. Flow regulation was achieved with a ball valve at the reactor inlet, and the pump operated on a 230 V power supply. The design allowed flexible configuration with 1 to 5 packed tubes connected in sequence, facilitating photocatalytic testing under varying reactor volumes, residence times and flow conditions.

The LED-IoT system was designed using COB BRIDGELUX (USA) Thrive series diodes (6500 K; CRI 97), which feature a low Average Spectral Difference (ASD) index of only 8 % compared to natural sunlight. The diodes were connected in series to ensure uniform illumination. The IoT control system included a Dim-DALI constant current driver (LL 1 × 10–42-*E*-DA, Helvar, Finland), a Bluetooth communication module (Hytronik, UK), and Passive Infrared Sensors (PIR, Hytronik, UK), enabling real-time regulation of radiation intensity based on ambient lighting conditions. The light source was configured using the LL ClueIN application (Android, Google Play Store) via the Daylight Harvest mode, setting the target insolation value for the photoreactor at 20,000 lx. Fig. S1 (see SI) present images of the individual system components. The aluminium light housing acts both as a thermal sink and optical collimator, while the COB LEDs produce a focused, downward light distribution that ensures uniform illumination along the 12 cm active length of each reactor tube, thereby improving photon delivery even in radial configurations.

2.4.2. Photocatalyst activity testing

Details of the photocatalytic activity tests, including solution preparation, reactor operating conditions, sampling strategy, UV–Vis analysis, mass spectrometry (ESI-MS), and ecotoxicity evaluation using ECOSAR software, are provided in the Supplementary Information. Photocatalytic experiments were conducted in both Palermo (Italy) and Poznań (Poland) under differing solar radiation conditions to validate system performance across environmental scenarios. While absolute spectral measurements were not the primary focus of this comparative study, the experiments were conducted under representative solar conditions at each location. The aim was to capture system behavior under realistic and geographically distinct irradiance profiles. Minor differences in UV-A and visible light exposure, due to seasonal and climatic variability, were mitigated by the inclusion of adaptive LED modules, ensuring reproducible activation of the photocatalyst.

2.4.3. Photocatalytic tests with real water matrices

Photocatalytic tests were also performed using real water matrices (tap water, municipal wastewater, and hospital sewage), each spiked with 20 mg L^{-1} of NPX. Details regarding sample collection, water quality parameters, and experimental procedures, including prefiltration and light-protected storage, are provided in the Supplementary Information (Table S1). These tests aimed to evaluate the system's applicability under real-world conditions using consistent analytical protocols.

3. Results and discussion

3.1. Physicochemical characterization of TiO_2-based bioinspired photocatalysts

The structural and chemical properties of the synthesized photocatalysts were examined by XRD, SEM, HR-TEM, EDX and XPS to determine the crystal structure, the morphology and the surface composition.

Luffa cylindrica sponge was primarily composed of cellulose, as evidenced by the XRD diffraction peaks (Fig. 1a) corresponding to the (101) and (002) planes of cellulose (ICDD card no. 00–003-0226) [19]. In contrast, the XRD pattern of the marine sponge exhibited a predominantly amorphous character, consistent with its composition being primarily based on spongin protein, which lacks a crystalline structure [20] (Fig. 1b). However, a minor additional peak was observed, likely corresponding to residual silica (SiO_2), a common component of marine sponge skeletons. This peak reflects the natural origin of the material and may be attributed to incomplete removal of inorganic phases, despite applying the cleaning procedure described by Żółtowska et al. [21,22].

In the synthesized photocatalysts, additional diffraction peaks were observed at $2\theta = 25.5°$, 36.7°, 48.3°, 54.2°, 55.3°, 63.0°, 68.1°, 70.8°, and 75.3°, corresponding to the anatase phase (ICDD card no. 21–1272). These reflections are attributed to the (101), (004), (200), (105), (211), (204), (116), (220), and (215) planes of anatase, respectively [18]. Detailed HR-TEM analysis of the TiO_2 nanoparticles deposited on both supports (Fig. 2a) confirms their high crystallinity and the presence of the anatase phase, as evidenced by interplanar spacing measurements and FFT patterns [23].

SEM images of the bare sponge (Fig. 2b) revealed fibers with an average diameter of approximately 25 μm. The skeleton displayed a three-dimensional, reticular architecture composed of open-pore cellular networks and multi-junctional regions [21,22]. A comparable fibrous structure was observed in the *Luffa cylindrica* sponge, although its fibers were significantly thicker, measuring around 400 μm in diameter. Optical microscope images (Fig. S2 in the SI), captured at higher magnification, revealed the presence of surface impurities on both types of bare sponges, a common feature of natural skeletons due to their organic origin [23,24]. SEM analysis of the bioinspired photocatalysts confirmed a uniform deposition of TiO_2 nanoparticles on the sponge fibers in both materials. Importantly, the TiO_2 coating process did not compromise the structural integrity of the scaffolds. The three-dimensional architecture of both the marine sponge and *Luffa cylindrica* was preserved after functionalization, maintaining their open-pore cellular frameworks and multi-junctional regions. This structural stability is essential, as it allows the coated photocatalysts to retain the inherent advantages of biomimetic scaffolds, including high porosity and improved accessibility of reactants which are key factors for efficient photocatalytic activity. Further SEM imaging revealed morphological differences between the two materials: the marine sponge exhibited a noticeably thicker TiO_2 layer, with visible nanoparticle

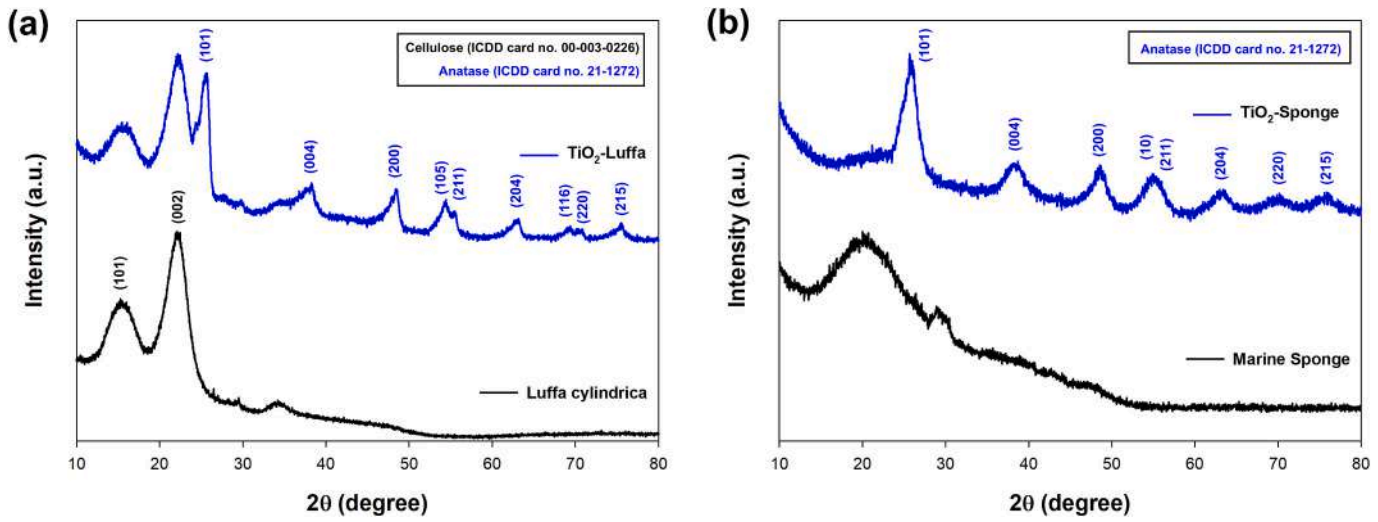

Fig. 1. The XRD patterns for photocatalysts based on (a) *Luffa cylindrica*, and (b) Marine sponge.

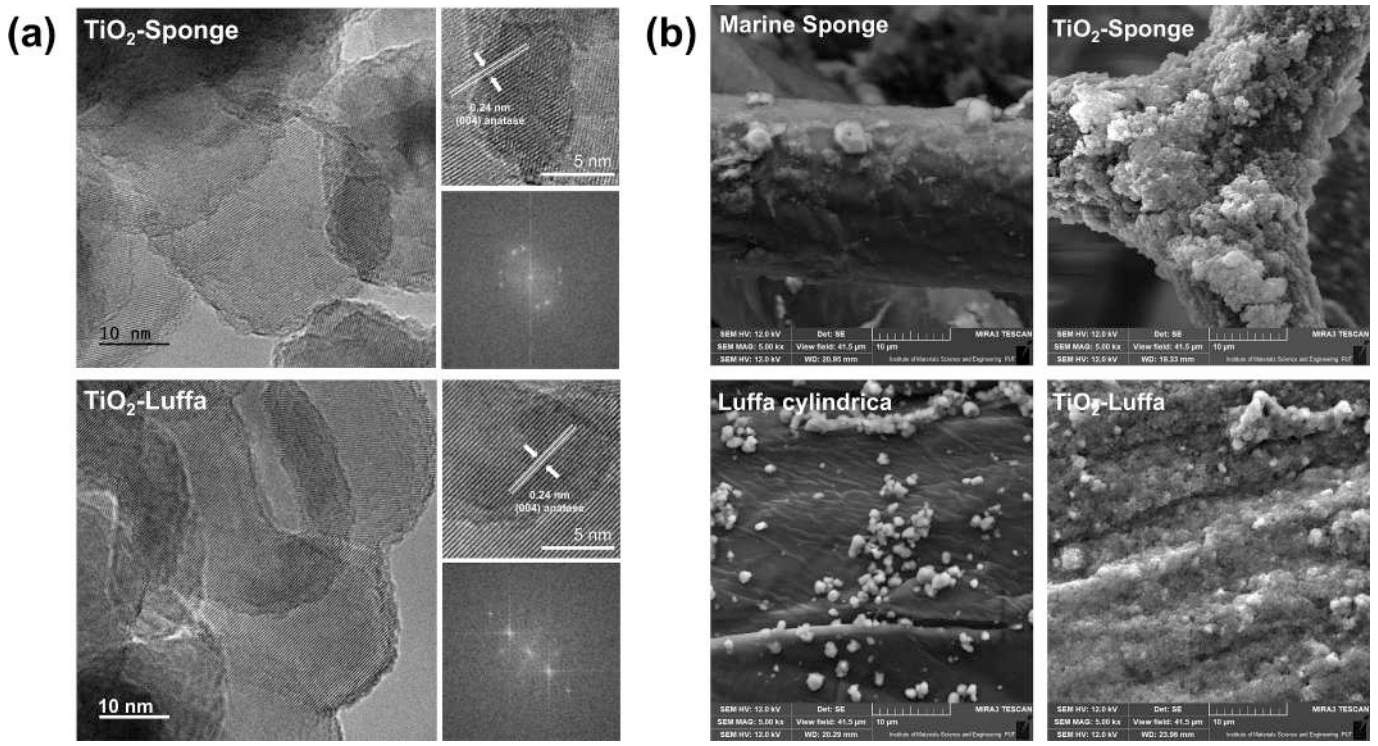

Fig. 2. (a) HR-TEM images of TiO_2 nanoparticles deposited on marine sponge and *Luffa cylindrica* supports. Insets show interplanar spacing of 0.24 nm corresponding to the (004) anatase phase and FFT patterns confirming high crystallinity; (b) SEM images of uncoated and TiO_2-coated scaffolds.

aggregates forming on the fiber surfaces, whereas the plant-based scaffold showed a more homogeneous and evenly distributed TiO_2 coating. This contrast can be attributed to the intrinsic physicochemical differences between the two scaffolds. Marine spongin is a proteinaceous biopolymer enriched in acidic and sulphated residues, which strongly coordinate Ti(IV) ions and promote high nucleation density, resulting in thicker coatings and local agglomerates. In contrast, the cellulose-rich Luffa framework interacts more weakly with Ti(IV) due to its predominantly neutral –OH groups, leading to a slower, more uniform deposition process. These scaffold-dependent interfacial effects explain the observed morphological differences in the SEM images.

EDX analysis (Fig. 3) confirmed the uniform distribution of TiO_2 nanoparticles on the surface of both sponge skeletons. EDX results indicate 25 % loading by weight of TiO_2 on the marine sponge scaffold, (see Fig. S3 in SI), which aligns with the mass gain measured after synthesis. In contrast, the Ti content on the surface of *Luffa cylindrica* was lower, at less than 20 % by weight (see Fig. S4 in SI). This observation is consistent with previous SEM results, which suggested differences in the coating thickness and distribution between the two bioinspired scaffolds.

Fig. 4 shows the XPS spectra for TiO_2-based bioinspired photocatalysts. The complete spectra for the reference sponge scaffold and the synthesized photocatalysts are provided in Fig. S5 in the SI. The spectrum in the C 1 s region was fitted with two components. The main C 1 s peak is dominated by the C—O bond type at 286.5 eV [25]. Additionally, the peak at 288.5 eV is characteristic of oxygen-bound species (O–C=O)

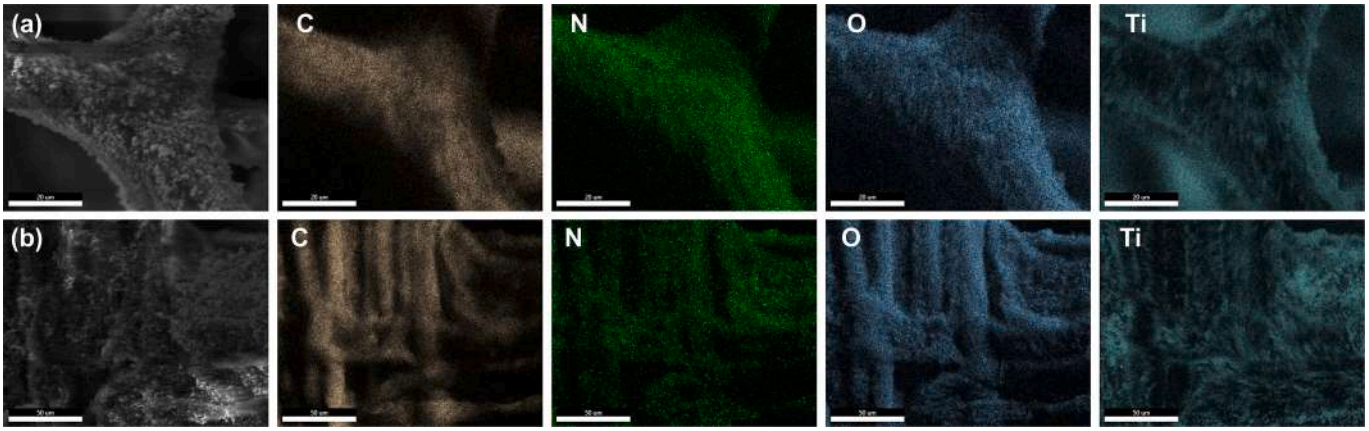

Fig. 3. EDX elemental mapping of (a) TiO_2-Sponge and (b) TiO_2-Luffa photocatalysts. From left to right, the maps represent the distribution of carbon, nitrogen, oxygen, and titanium.

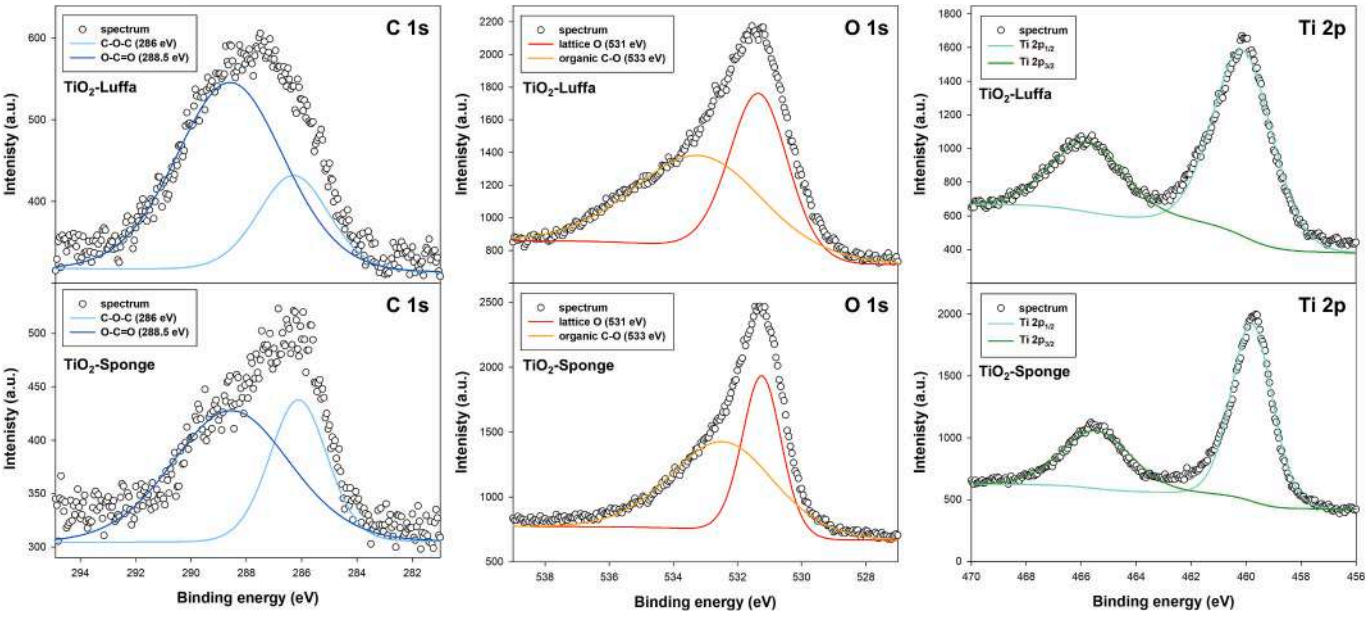

Fig. 4. XPS spectra of the C 1 s, O 1 s, and Ti 2p regions for TiO_2-based bioinspired photocatalysts.

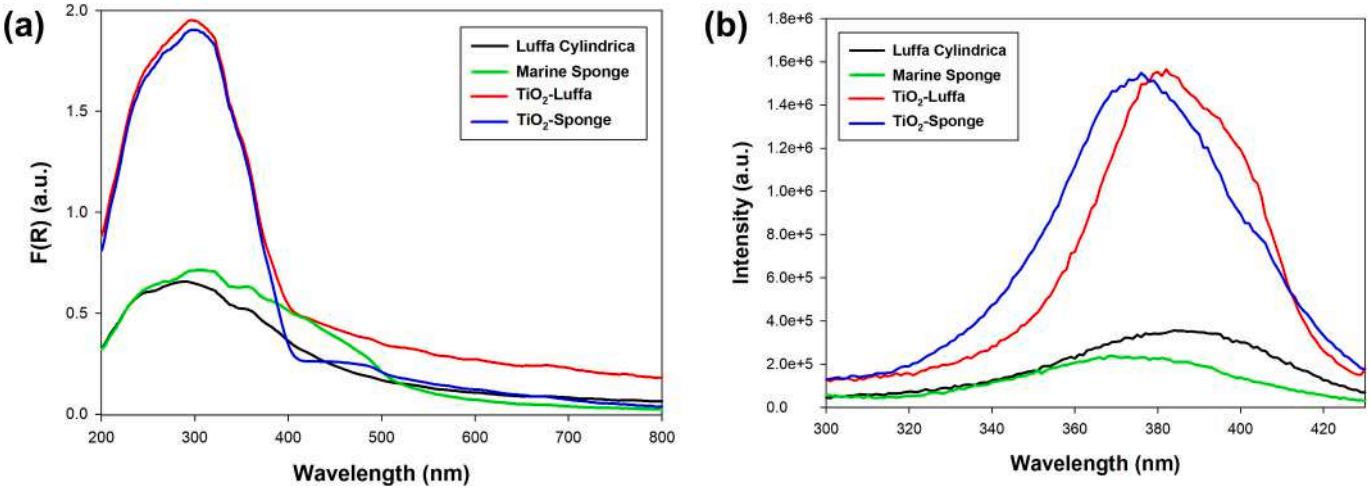

Fig. 5. (a) DRS and (b) excitation spectra for the reference sample and the TiO_2-based bioinspired photocatalysts.

[26]. These peaks originate from the organic structure of the biomimetic matrices [27]. Specifically, the organic composition of the scaffolds, such as cellulose in *Luffa cylindrica* or spongin in marine sponges, provides a source of carbon-oxygen functional groups. The O 1 s region of the spectra exhibits a double peak that can be deconvoluted into two distinct contributions: lattice oxygen (530.5 eV) and oxygen bound in the organic matrix (C—O, 533 eV) [28]. The Ti 2p region exhibits two characteristic peaks with binding energies centered at 459.3 eV and 465 eV, corresponding to Ti $2p_{3/2}$ and Ti $2p_{1/2}$, respectively [29]. The 5.7 eV splitting between Ti $2p_{1/2}$ and Ti $2p_{3/2}$ is consistent with the presence of Ti^{4+} in the anatase phase of TiO_2 [30]. Remarkably, the absence of Ti^{3+} states indicates that heteroatoms from the scaffold fibers are not incorporated into the TiO_2 crystal lattice.

3.2. Photocatalyst optical properties and integration with the flow-through LED-IoT photocatalytic system

The optical characterization aimed to assess the light absorption behavior of the synthesized materials, including their band gap energy and spectral response, to evaluate their potential for activation under tailored illumination conditions. Fig. 5 presents the diffuse reflectance spectra (DRS) of the reference sponge skeleton and the TiO_2-based bioinspired photocatalysts. The uncoated scaffolds exhibited weak absorption across a broad range of 200–600 nm, primarily attributed to their organic structure and the possible presence of heteroatoms capable of inducing low-intensity excitations. Upon TiO_2 deposition, a pronounced absorption edge appeared in the 200–400 nm region, characteristic of anatase-phase TiO_2 [31]. As determined from Tauc plot analysis (Fig. S6, SI), the estimated band gap energy for both bioinspired photocatalysts was approximately 3.1 eV, which is consistent with unmodified anatase. No measurable band gap narrowing was observed upon immobilization. However, the excitation spectra (Fig. 4b) revealed an enhanced spectral response above 400 nm, suggesting the presence of sub-bandgap electronic states.

These transitions are attributed to defect-related levels, primarily oxygen vacancies and Ti^{3+} centers, which can act as intermediate energy states within the band structure, extending the spectral sensitivity beyond the intrinsic absorption edge without altering the fundamental band gap. This behavior supports the formation of localized interface states, as observed in our previous study [18], as verified by EPR spectroscopy. Moreover, the contribution of these defect states to improved photoactivity is well established in the literature [32].

The innovative flow-through LED-IoT system in this study combines tailored photocatalytic materials with an optimized light delivery

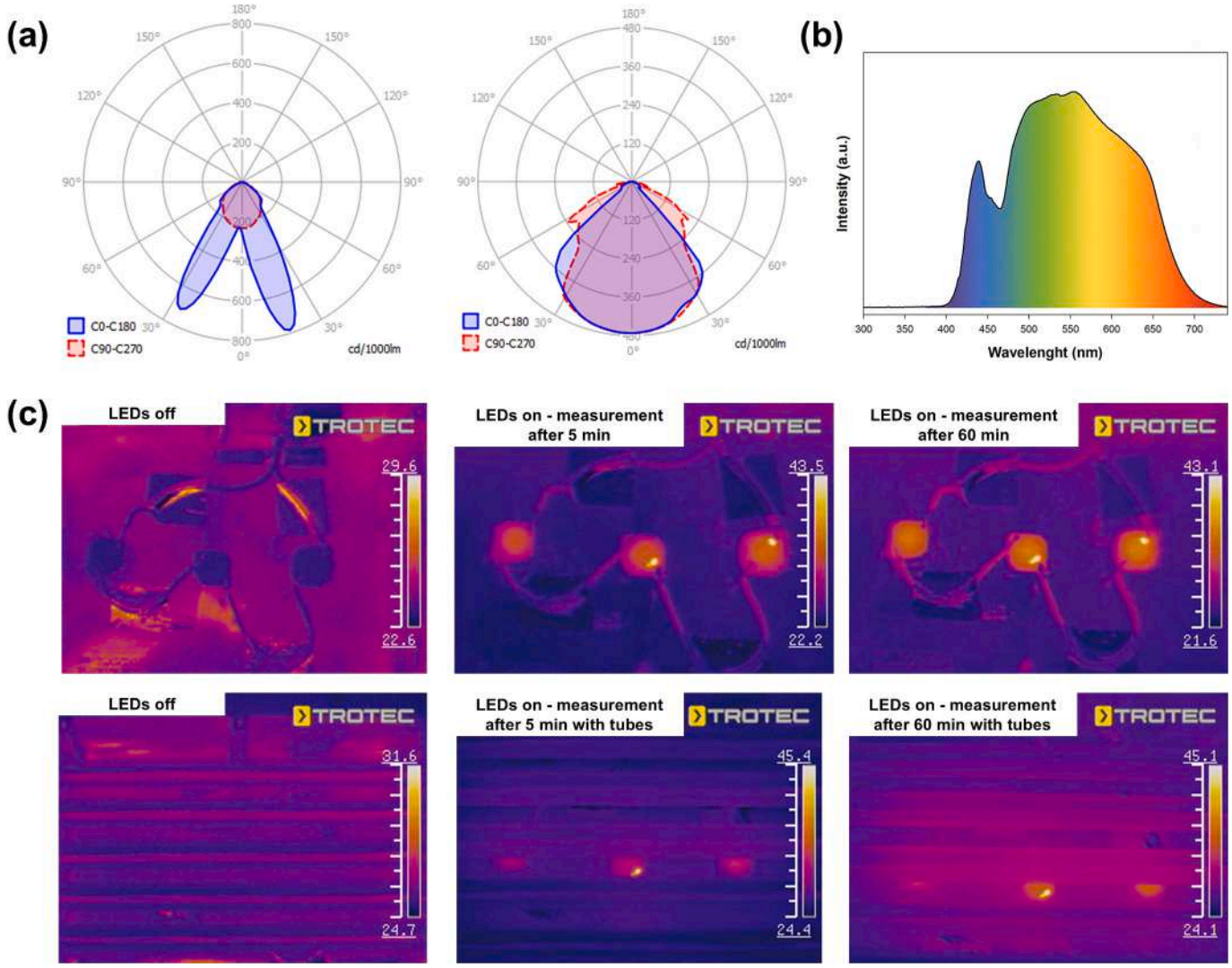

Fig. 6. (a) Angular light distribution of the LED system: (left) with tubes containing the photocatalyst and (right) without tubes. (b) Emission spectrum of the LED system. (c) Thermal imaging of the LED system: (top) measurements without tubes and (bottom) measurements with tubes, showing temperature distribution with LEDs off, after 5 min, and after 60 min of operation.

strategy, reflecting a comprehensive approach to photocatalytic system design developed through our earlier research efforts. Fig. 6 provides a comprehensive analysis of the parameters of the developed LED light source, including the spectral characteristics, light distribution, and thermal performance as assessed through thermal imaging. Fig. 6a shows the angular light distribution of the LED system, when the tubes containing the photocatalyst are packed in the reactor (left diagram) and in their absence. In the first case, a more concentrated and directional light pattern was observed, likely due to the refraction and scattering effects caused by the tubes. This focused distribution ensures that the light is effectively confined to the reaction zone, enhancing photon delivery to the photocatalyst. In contrast, in the absence of the tubes a broader and more uniform angular light spread was determined, with light emitted freely in all directions. This comparison demonstrated that the photoreactor design effectively focuses the light emitted by the LED source, which is critical for improving the overall efficiency of the photocatalytic process.

Fig. 6b shows the emission spectrum of the additional LED light

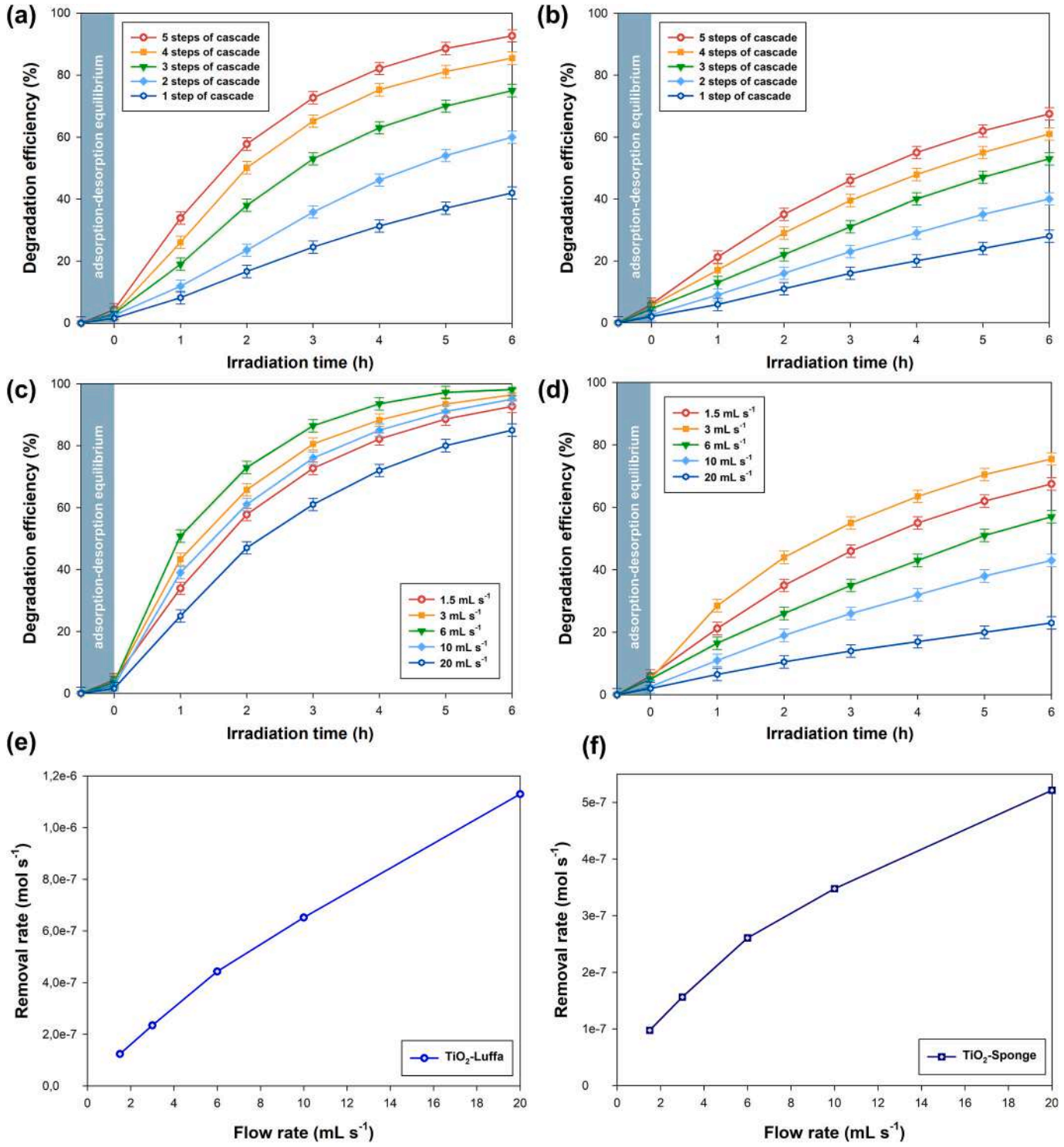

Fig. 7. NPX photodegradation using (a,c) TiO_2-Luffa and (b,d) TiO_2-Sponge photocatalysts: (a,b) depict the optimization of the cascade stage; (c,d) focus on the flow rate; (e) and (f) present the removal rate (mol s^{-1}) as a function of flow rate.

source used in the photocatalytic system. Bridgelux Thrive LEDs were specifically selected for their deviation of no more than 8 % from sunlight; this allowed to minimize possible spectral differences which may introduce variations in the degradation mechanism, ensuring consistency and reliability in photocatalytic performance.

Fig. 6c shows the evaluation of the temperature stability of the LED system under various operating conditions. Measurements were performed with the LEDs turned off, after 5 min of operation, and after 60 min, both with and without tubes. When the LEDs were off, the system remained at ambient temperature. After 5 min of LED operation, the LED chips reached a stable temperature of approximately 45 °C demonstrating excellent thermal stability, while the tubes showed no noticeable heating, maintaining a temperature of around 25–26 °C. The aluminium structural base of the photoreactor system effectively dissipated the LED heat. The tubes, on the other hand, exhibited a slight temperature increase after 60 min, reaching around 30–32 °C, likely due to prolonged exposure to the surrounding environment. Importantly, this minor temperature increase did not negatively affect the photocatalytic process since a temperature rise above 70 °C is required to significantly increase charge carrier recombination [33].

3.3. Photocatalytic activity

The performance of the flow-through tubular photocatalytic reactor, incorporating the TiO_2-Luffa or TiO_2-Sponge open-structured photocatalysts, was evaluated through the degradation of spiked NPX in deionized water as well as in tap, municipal, and hospital wastewater. The influence of key operational parameters, including the number of irradiated tubes and the system flow rate, was systematically investigated to determine optimal conditions and assess the reaction kinetics.

An investigation into the optimal number of reactor tube stages reveals a complex relationship between photocatalytic process efficiency and the required duration for pollutant removal, as illustrated in Fig. 7a and b. To validate the mechanistic assumptions underlying the modular flow-through photocatalytic system, a kinetic analysis based on the packed-bed plug flow reactor model was conducted. The mole balance for a differential reactor volume is expressed as:

$$\frac{dF_A}{dV} = r_A \tag{1}$$

where F_A (mol s^{-1}) is the molar flow rate of the reacting species A (in this case NPX). Assuming pseudo-first-order kinetics, the rate of reaction per unit reactor volume of the packed bed is:

$$-r_A = kC_A \tag{2}$$

Substituting Eq. (2) into Eq. (1) and integrating over the reactor volume yields the following expression for the apparent rate constant k (s^{-1}),:

$$k = \frac{1}{\tau}\ln\left(\frac{C_{A0}}{C_A}\right) \tag{3}$$

where τ is the space time (s), C_{A0} and C_A are the initial and final concentrations of NPX (mol m^{-3}). The apparent rate constant per unit mass of catalysts ($m^3\ kg^{-1}\ s^{-1}$) is $k' = k/\rho_b$ where ρ_b is the bulk density of the catalyst (kg m^{-3}).

The calculated values of k for different tubular packed reactors in series configurations (1 to 5 modules, Table S2 SI) show independence on the number of modules as expected for apparent 1st-order reaction. The apparent rate constant with the TiO_2–Luffa system was approximately 0.062 s^{-1} corresponding to k' of $3.13 \cdot 10^{-4}$ $m^3\ kg^{-1}\ s^{-1}$. In contrast, the TiO_2-Sponge system exhibited significantly lower kinetic constants, with k approximately equal to 0.026 s^{-1} and k' $1.57 \cdot 10^{-4}$ $m^3\ kg^{-1}\ s^{-1}$. The uniformity of values confirms that the system adheres to ideal plug flow reactor kinetics. The differences in photocatalytic efficiency among the two TiO_2 scaffolds was attributed to the structural characteristics of the two supporting matrices. *Luffa cylindrica*'s open-pore architecture allows deep light penetration and efficient flow-through contact, enhancing species mass transfer and TiO_2 photoactivation. Additionally, its fibrous surface supports a uniform TiO_2 coating, maximizing the active surface area. In contrast, light penetration through the sea sponge's denser structure is more difficult, and SEM analysis revealed TiO_2 aggregation forming thicker less accessible coatings. The multi-stage configuration further emphasized the advantages of the Luffa-based material, enabling near-complete NPX removal. These findings highlight the crucial role of matrix morphology and porosity in optimizing photocatalytic performance in continuous-flow systems operating under environmentally realistic parameters. Although the LED array positioned beneath the borosilicate tubes limits the optical pathlength to approximately 13 mm, thereby ensuring a high average photon flux across the irradiated zone, the inherently complex three-dimensional architecture of the bio-derived scaffolds gives rise to internal microdomains with reduced light accessibility. As a result, a fraction of TiO_2 crystallites embedded within the narrower and more tortuous pore network of the marine sponge may experience suboptimal irradiance, contributing less effectively to the overall photocatalytic process than those located on the more exposed surface regions. This self-shading effect is less pronounced in the case of *Luffa cylindrica*, whose wider and straighter channels promote more uniform light distribution and activation of the immobilized photocatalyst. The observed differences in apparent rate constants between the two scaffolds thus likely reflect not only morphological and hydraulic characteristics, but also the extent of internal photon attenuation. Acknowledging this limitation, future work will focus on tuning scaffold porosity and refining the light delivery architecture to further minimize internal shading while maintaining the structural integrity and sustainability advantages of bio-based supports.

Fig. 7c and d summarize the results of photocatalytic performance as a function of flow rate for TiO_2-Luffa and TiO_2-Sponge systems. In addition to degradation efficiency, the apparent reaction rate constants k and mass-normalized constants k' were calculated for each flow condition based on the packed-bed plug flow reactor model; the resulting kinetic parameters are compiled in Table S3 of the SI. In the TiO_2-Luffa system, the highest degradation efficiency (>90 %) was achieved at a flow rate of 6 mL s^{-1}, where an optimal balance between residence time and convective mass transfer was observed. The apparent reaction rate constant k increased steadily with increasing flow rate, from 0.0622 s^{-1} at 1.5 mL s^{-1} to 0.6324 s^{-1} at 20 mL s^{-1}, confirming enhanced reaction kinetics driven by improved pollutant mass transfer. Correspondingly, the mass-normalized rate constant k' rose from $3.12 \cdot 10^{-4}$ to $3.18 \cdot 10^{-3}$ $m^3\ kg^{-1}\ s^{-1}$ across the tested range. Despite this kinetic improvement, a gradual decline in overall degradation efficiency was observed at flow rates above 6 mL s^{-1}. For instance, the efficiency dropped to approximately 85 % at 10 mL s^{-1} and 70 % at 20 mL s^{-1} This reduction is attributed to the shortened residence time (e.g., 3.93 s at 20 mL s^{-1}), which limits the duration of contact between the pollutant and the photocatalyst, despite faster reaction kinetics. To better reflect the practical removal capacity of the system, the removal rate was calculated using the following equation:

$$\textit{Removal rate} = C_{A0} \times \left(\frac{\textit{Degradation efficiency}}{100}\right) \times \textit{Flow rate} \tag{4}$$

where C_{A0} is the influent concentration (20 mg·L^{-1}) and the flow rate was converted from mL s^{-1} to L h^{-1}. For the TiO_2-Luffa system, the resulting removal rates were 99.4, 208.2, 424.4, 684.0, and 1224.0 mg h^{-1} at flow rates of 1.5, 3, 6, 10, and 20 mL s^{-1}, respectively. These results highlight that, although degradation efficiency slightly decreases at higher flow rates, the overall mass of pharmaceuticals removed per unit time increases significantly due to increase in the rate of mass transfer.

The TiO_2-Sponge system exhibited overall lower degradation efficiencies across all flow rates, with a maximum of ~70 % achieved at 3

mL s^{-1}. The rate constant k increased from 0.0263 s^{-1} at 1.5 mL s^{-1} to 0.0844 s^{-1} at 6 mL s^{-1}, and continued to increase with higher flow rates, indicating that the system was not yet limited by mass transfer. Similarly, the apparent rate constant k' also increased, supporting the conclusion that improved flow enhances photocatalytic performance through better mass transport. This is likely due to structural constraints, such as dense pore architecture and aggregated TiO_2 layers, which restrict light penetration and active site accessibility. Additionally, turbidity observed at higher flow rates may indicate partial detachment of TiO_2 particles, further compromising performance. The corresponding removal rates for the TiO_2-Sponge system were 70.9, 163.1, 246.2, 309.6, and 331.2 mg h^{-1}, confirming a less efficient yet still flow-dependent removal trend. This comparative analysis illustrates that removal rate offers an insightful operational parameter complementing degradation efficiency, especially in evaluating system scalability and throughput.

To further understand the influence of flow rate on pollutant transport, Sherwood numbers were calculated, reflecting the ratio of convective to diffusive mass transfer [34,35]. Sherwood number estimation, are provided at the SI. The Sherwood number for the TiO_2-Luffa system increased significantly with flow rate, from 221 at 1.5 mL s^{-1} to 885 at 6 mL s^{-1}, and further to 2950 at 20 mL s^{-1}. This substantial increase indicates that higher flow rates` enhance mass transfer efficiency, facilitating the delivery of NPX to the photocatalyst surface and supporting the improved degradation observed at 6 mL s^{-1}. As Sherwood numbers increase, the dominance of convective transport over molecular diffusion becomes evident, enhancing the availability of pollutants to the photocatalytic surface. Despite the continuous increase in Sherwood number with flow rate, indicative of enhanced convective mass transfer, the concomitant reduction in residence time at higher flow velocities limited the effective interaction time between the pollutant and the photocatalyst surface, ultimately leading to a decline in degradation efficiency [36]. In the case of the TiO_2-Sponge system, Sherwood numbers exhibited a comparable trend, increasing with flow rate due to intensified convective transport. However, the inherent structural limitations of the marine sponge matrix attenuated the practical benefits of improved mass transfer. Specifically, although higher flow rates facilitated more efficient pollutant delivery to the catalyst surface, the observed detachment of TiO_2 particles above 6 mL s^{-1} impaired photocatalytic performance. This phenomenon suggests that the thicker TiO_2 layers formed on the sponge scaffold were not sufficiently anchored and became susceptible to mechanical erosion under intensified hydrodynamic conditions. To provide a more operationally relevant assessment of system performance, the removal rate (mg h^{-1}) defined as the product of influent concentration, degradation efficiency, and volumetric flow rate was introduced as a complementary performance metric. While degradation efficiency decreased at higher flow rates, the corresponding removal rate consistently increased, reflecting the higher mass throughput of treated pollutant per unit time. This underscores that the benefits of enhanced mass transfer can only be fully exploited when photocatalyst immobilization is mechanically robust and resilient to shear forces. The full set of calculated Sherwood numbers is reported in Table S4 in SI.

The reusability test was conducted over five consecutive cycles of NPX photodegradation to evaluate the efficacy and durability of the cascade photocatalytic system, as illustrated in Fig. S7 in SI. The TiO_2-Luffa photocatalyst was selected for this test due to its superior photocatalytic efficiency compared to the TiO_2-Sponge system. At the end of each cycle, the degraded sewage solution was removed using a submersible pump and replaced with fresh sewage solution. Notably, no additional cleaning or regeneration of the photocatalyst was performed between cycles. Importantly, the pumped solution remained clear throughout the test, indicating that the TiO_2 coating remained securely bound to the spongin-based matrix, with no evidence of particle detachment. The photocatalytic degradation efficiency remained consistent across all five cycles, with no significant decline in performance. These results demonstrate the high stability and reusability of the designed photocatalytic system, highlighting its potential for long-term applications in wastewater treatment.

To assess the possible loss of TiO_2 from the photocatalyst surface, XPS analysis was performed after five photocatalytic cycles (Fig. S8, SI). The survey spectra and high-resolution Ti 2p region showed no detectable loss of titanium from the surface. The atomic percentage of Ti decreased only marginally from 12.6 % to 11.8 %, which falls within the expected analytical variability and confirms the absence of significant leaching. Additionally, the Ti $2p_{3/2}$ and Ti $2p_{1/2}$ binding energies remained unchanged, indicating the preservation of the Ti(IV) oxidation state and surface chemistry. The elemental composition of oxygen and carbon also remained nearly constant. These results confirm that the photocatalyst retains both its chemical identity and interfacial stability upon repeated use, supporting its suitability for long-term deployment in aqueous environments.

3.4. Validation of the LED-IoT photocatalytic system under different climatic conditions

The LED-IoT photocatalytic system was operated under two markedly different natural-irradiation regimes: Palermo, Italy, in May 2024, where the average sunshine duration was approximately 9 h day^{-1}, and the daily global solar radiation increased from about 6.6 to 7.5 kWh m^{-2} over the month; and Poznań, Poland, in October 2024, where the average sunshine duration was only 3–4 h day^{-1}, and the daily solar radiation remained below 1.7 kWh m^{-2}. These conditions were chosen to verify whether the proposed solution, based on IoT sensors, would function effectively regardless of location and environmental conditions. The LED module was automatically triggered by IoT sensors when ambient irradiance dropped below a predefined threshold corresponding to the average solar intensity. This configuration ensured that the photocatalytic process received a consistent light input throughout the day, even under overcast skies or during early morning and late afternoon hours.

Fig. 8 presents a comparison of photocatalytic efficiencies obtained in the NPX photooxidation process conducted in different locations using the bioinspired TiO_2-Luffa and TiO_2-Sponge photocatalysts. The results indicate that the proposed LED-IoT solution enables effective photodegradation regardless of location. However, in the tests conducted in October in Poznan, Poland, a decrease in efficiency of approximately 8–11 % was observed compared to the tests conducted in Palermo, Italy.

This decrease in efficiency can be attributed to several factors. Firstly, during the tests in Palermo, the LED-IoT system was rarely activated due to the high levels of natural sunlight. The PIR daylight sensor continuously monitored sunlight levels and only triggered the LED system when the measured sunlight intensity fell below the pre-set threshold, such as when the installation was shaded by surrounding buildings. In contrast, during the tests in Poznan, the significantly lower sunlight intensity typical of October required the LED-IoT system to compensate for the lack of natural sunlight much more frequently. Another critical factor was the differences is the spectral composition of sunlight irradiation in both locations. The photocatalyst used in this study, TiO_2 modified with carbon, was designed to operate under the UV–visible light spectrum (Fig. 5). However, since TiO_2 activity in the UV is much higher than in the visible, the much higher UV index in Palermo (up to 9 in May) compared to Poznan (around 1–2 in October) contributed to differences in activity in the two locations. This lack of UV activation in Poznan, combined with shorter daylight hours, placed greater reliance on the LED-IoT system, which generates only visible light and cannot replicate the effects of UV-induced activation. While the PIR sensor used in the system has a short reaction time, it is also important to consider the configured delay time. In this installation, the delay time was set to 10 s, meaning that the sensor monitored solar radiation parameters for a continuous interval before sending a signal to

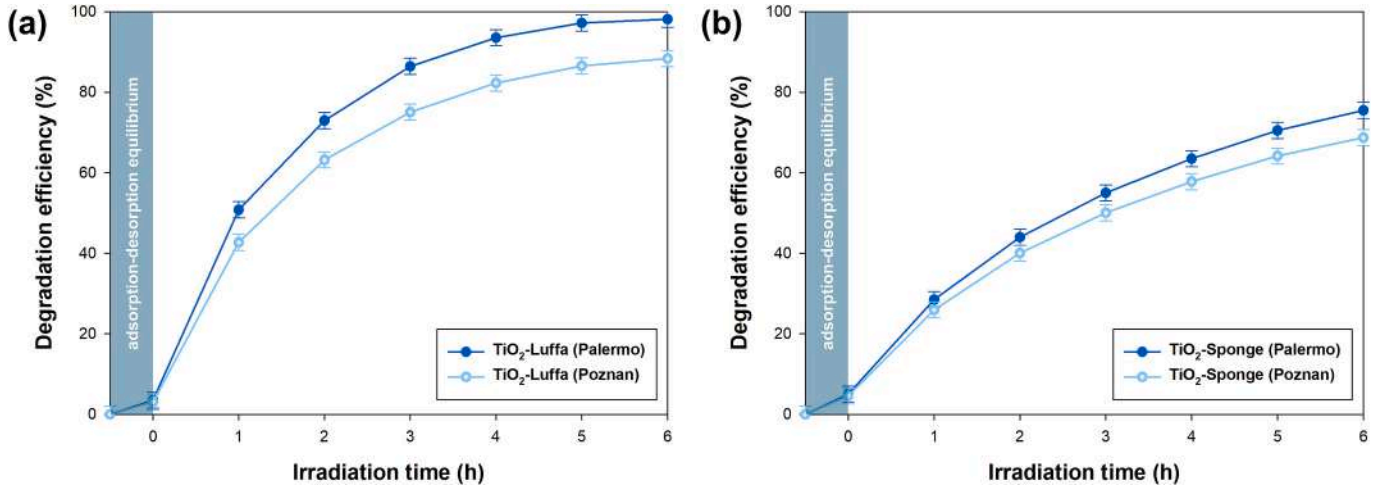

Fig. 8. Results of photocatalytic tests conducted in two locations: Palermo, Italy, and Poznan, Poland, using the LED-IoT photocatalytic system based on (a) TiO_2-Luffa and (b) TiO_2-Sponge photocatalysts.

activate the LEDs. This configuration ensures stable readings and prevents the system from reacting too frequently to brief sunlight fluctuations, such as those caused by passing clouds. However, in conditions with rapidly variable sunlight near the pre-set activation threshold, this delay may introduce slight inefficiencies, particularly in Poznan's low-sunlight environment. Despite these tuning challenges, the LED-IoT system effectively compensated for the reduced sunlight in both locations, ensuring robust photocatalytic performance even under less favorable conditions in Poznan.

3.5. Integrated evaluation of system performance: real-world applicability, and environmental safety

The critical part of this research focused on applying the LED-IoT system based on the TiO_2-Luffa photocatalyst in real-world scenarios. Three water matrices were selected for testing: tap water, municipal wastewater, and hospital wastewater. Pharmaceuticals in tap water arise from the infiltration of surface and groundwater by untreated wastewater, leading to their occasional detection even in treated water [37]. Municipal wastewater contains a significant load of pharmaceuticals excreted in unaltered or slightly modified forms, which conventional treatment processes fail to remove effectively [38]. Hospital wastewater poses the greatest challenge due to the high concentration and variety of pharmaceuticals discharged, emphasizing the urgent need for advanced treatment technologies [39]. This study aimed to evaluate the system's effectiveness in addressing these contamination challenges.

Fig. 9 presents the photocatalytic degradation efficiency of NPX in three real aqueous matrices: tap water, municipal wastewater, and hospital wastewater, evaluated using the modular flow-through photocatalytic reactor packed with TiO_2-Luffa. The degradation behavior was interpreted using the packed-bed plug flow reactor model.

Tap water exhibited the highest NPX degradation efficiency, remaining just below 90 %, which closely aligns with the performance observed in demineralized water. This high efficiency can be attributed to excellent optical clarity and the absence of dissolved organic matter or interfering ions. The calculated apparent rate constant k was 0.2617 s^{-1}, and the mass-normalized rate constant k' reached $1.31 \cdot 10^{-3}$ m^3 kg^{-1} s^{-1}, confirming rapid reaction kinetics under ideal conditions. The removal rate, calculated as the product of influent concentration, degradation efficiency, and flow rate, was 401.9 mg h^{-1}, further emphasizing the suitability of the system for low-complexity water matrices. This result was further confirmed by COD removal efficiency, which reached 60.9 % in tap water and 68.8 % in demineralized water, indicating substantial mineralization of the organic load under these conditions. In municipal wastewater, the degradation efficiency decreased to 60 %, with a corresponding k value of 0.1124 s^{-1} and k' of

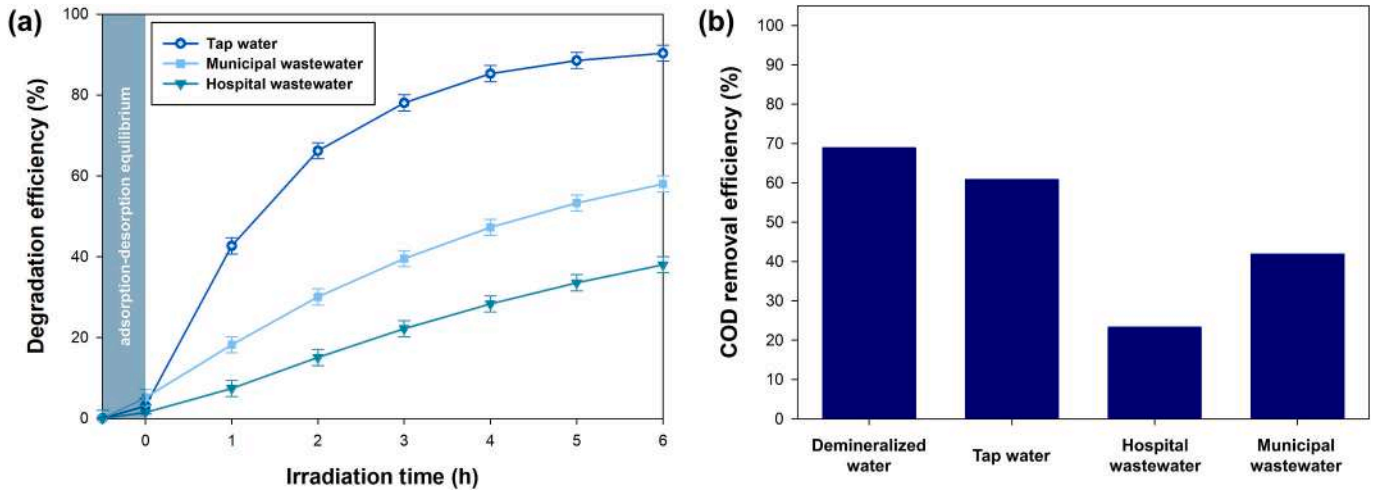

Fig. 9. (a) Photocatalytic degradation efficiency of NPX over time in different real water matrices using the TiO_2-Luffa photocatalytic system. (b) COD removal efficiency (%) in different real water matrices after photocatalytic treatment.

$5.64 \cdot 10^{-4}$ m^3 kg^{-1} s^{-1}. The reduction is mainly attributed to the presence of suspended solids, dissolved organic compounds, and background ions that interfere with light penetration and scavenge reactive oxygen species. Nonetheless, the removal rate remained significant at 292.5 mg h^{-1}, demonstrating that despite matrix complexity, the system maintained effective throughput under continuous flow conditions. The COD removal efficiency for municipal wastewater reached 41 %, further supporting the observed degradation performance and validating the system's applicability under moderate organic load. Hospital wastewater exhibited the lowest degradation efficiency near to ~40 %, with k equal to 0.0545 s^{-1} and k' equal to $2.74 \cdot 10^{-4}$ m^3 kg^{-1} s^{-1}. The substantial performance loss is linked to the complex composition of the matrix, which includes elevated levels of pharmaceuticals, macromolecular organic compounds, and various inorganic ions. These factors not only absorb incident photons but also deactivate photocatalytic sites or compete with NPX for reactive species. The resulting removal rate was 182.1 mg h^{-1}, indicating that while overall efficiency was reduced, the system still enabled significant pollutant reduction. Consistently, the COD removal efficiency in hospital wastewater was the lowest among all tested matrices (23 %), underscoring the challenge posed by high background contamination. These COD results align with NPX degradation trends and provide complementary evidence for the system's capacity to reduce total organic load.

These findings suggest that the TiO_2-Luffa photocatalytic system demonstrates notable robustness across various real-world water matrices. Although reduced performance was observed in more complex conditions, the system consistently retained functional activity, indicating its potential suitability for practical wastewater treatment

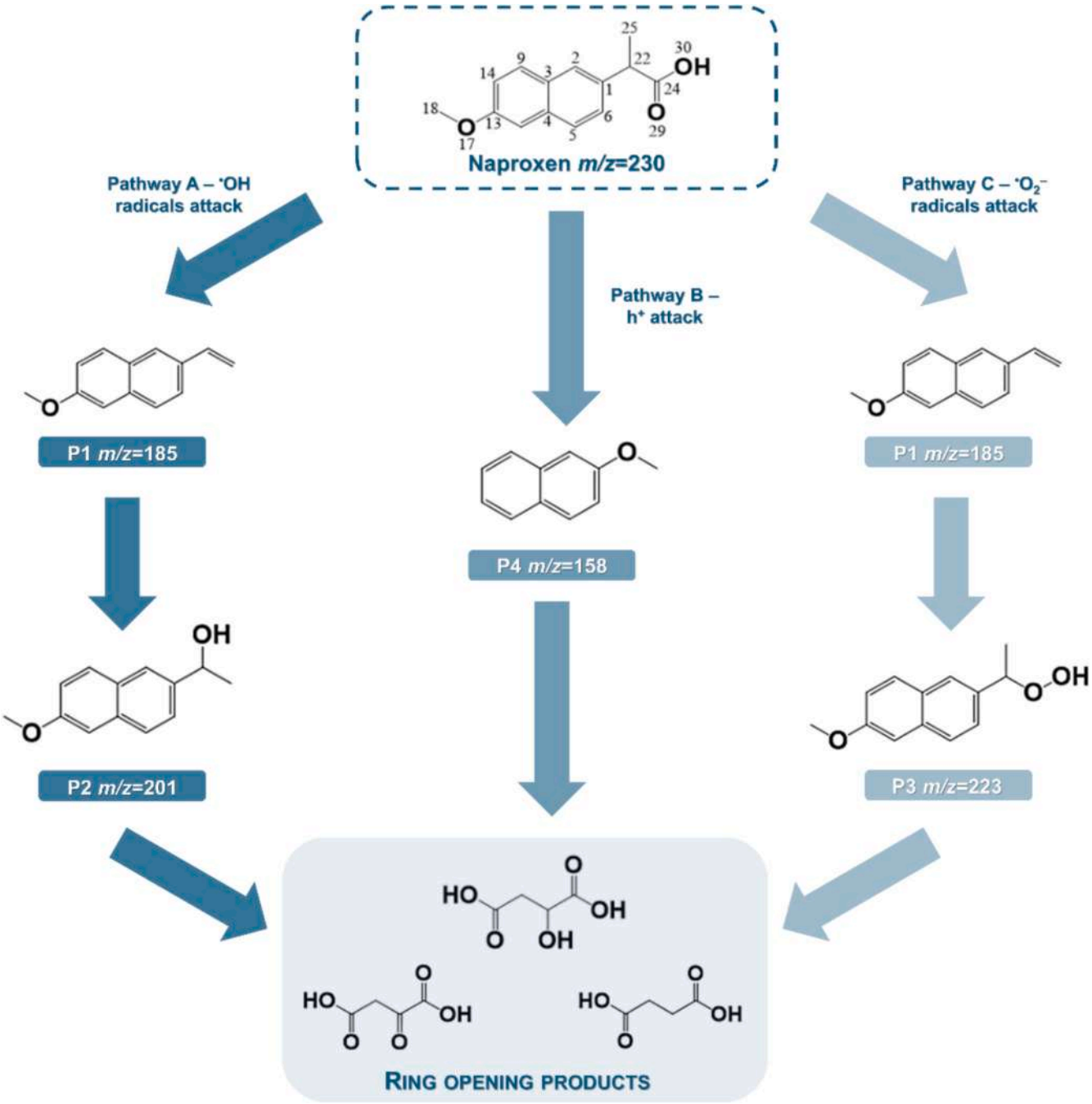

Fig. 10. The proposed degradation mechanism of NPX using LED-IoT cascade photocatalytic system.

applications.

The subsequent phase of this study focused on analyzing the degradation products generated during the photocatalytic process. Electrospray ionization mass spectrometry (ESI-MS) was employed to detect and identify these products, with experiments conducted in model solutions to ensure precise and reproducible conditions for elucidating the degradation pathways. This approach facilitated the identification of key intermediates and provided critical insights into the mechanisms underlying the degradation process. The MS spectral data supporting these findings are presented in Table S5 of SI.

The proposed degradation pathway, shown in Fig. 10, indicates that NPX degradation in the cascade photocatalytic system begins with a decarboxylation reaction. Hydroxyl radicals ($^{\bullet}OH$) initiate the process by attacking the methyl position of the naphthalene ring, leading to the formation of P1 (*m/z* 185) via hydrogen abstraction or addition at the α-carbon of the side chain, followed by β-scission and release of CO_2 [40]. This generates a 2-(6-methoxynaphthyl)benzyl radical, which is rapidly oxidized to P1 [41]. Rebound oxidation of the hydroxyalkyl intermediate prior to decarboxylation leads to P2 (*m/z* 201) [42]. Alternatively, valence band holes (h^+) or superoxide radicals ($^{\bullet}O_2^-$) can initiate the process by targeting carbon atoms with the highest positive charge. These interactions result in the formation of carbon-centered radicals, which undergo further decarboxylation and are transformed by ($^{\bullet}O_2^-$) into P1 (*m/z* 185) and P3 (*m/z* 223) [43]. Another pathway involves direct decarboxylation via h^+ attacking the C(1) position, producing P4 (*m/z* 158) [44]. Subsequent reactions include ring-opening mechanisms, yielding intermediates with *m/z* values of 131, 149, and 177, which are ultimately oxidized into CO_2 and H_2O [40].

The ESI-MS analysis was essential not only for elucidating the degradation pathway but also for enabling the subsequent evaluation of the ecotoxicity of the identified degradation products. The ecotoxicity assessment, conducted using ECOSAR software, focused on predicting the potential environmental impacts of these products, with particular emphasis on the LC50 parameter for aquatic organisms [45]. This integrated approach provides a comprehensive understanding of the degradation process and its implications for environmental safety.

The predicted acute toxicity of NPX and its transformation products was assessed. NPX itself exhibited an LC50 of 193 mg L^{-1}, indicating relatively low acute toxicity to aquatic organisms. However, the degradation products demonstrated varying levels of toxicity, with some intermediates showing significantly higher toxicity than the parent compound. Among the identified products, P1 (*m/z* 185) exhibited the highest toxicity, with an LC50 of 1.77 mg L^{-1}, classifying it as harmful to aquatic organisms. P4 (*m/z* 158) also showed increased toxicity with an LC50 of 9.8 mg L^{-1}, while P2 (*m/z* 201) and P3 (*m/z* 223) exhibited moderate toxicity, with LC50 values of 35.2 mg L^{-1} and 24.7 mg L^{-1}, respectively. In contrast, the ring-opening products displayed negligible toxicity, with LC50 values predicted to be extremely high, ranging from $2.89 \cdot 10^5$ mg L^{-1} to $1.40 \cdot 10^7$ mg L^{-1}. These intermediate ring-opening products pose minimal ecological risk.

The ECOSAR analysis highlights that while the photocatalytic degradation of NPX reduces the concentration of the parent compound, it generates intermediate products with varying toxicity levels. The significant toxicity of TP1, in particular, raises concerns about the potential ecological impacts of incomplete degradation in real wastewater systems. However, the negligible toxicity of the final ring-opening products underscores the importance of achieving complete mineralization of intermediates to mitigate environmental risks. These findings emphasize the need to optimize the photocatalytic process to ensure the effective transformation of harmful intermediates into non-toxic end products. This analysis provides valuable insights into the balance between degradation efficiency and the ecological safety of generated by-products, contributing to the development of sustainable photocatalytic systems for the treatment of pharmaceutical-contaminated wastewater.

Comparison of the system with pre-existent technologies was carried out through a comprehensive literature review to evaluate the efficiency of the developed LED-IoT system against previously reported photocatalytic approaches for NPX degradation in wastewater. The findings of this analysis are summarized in Table 1 and serve to validate the performance of the proposed system, while also emphasizing its novelty and advantages. The results demonstrate that the developed system offers competitive or superior performance, particularly under visible light conditions, supporting its applicability in sustainable wastewater treatment.

Table 1 summarizes representative strategies reported in the literature for NPX removal from wastewater, including adsorption, biodegradation, and photocatalysis. Adsorption processes, such as those involving GO-MNPs-SiO_2 composites, have achieved up to 85 % efficiency in batch systems [46]. Biodegradation in pilot-scale activated sludge systems has shown removals exceeding 90 % under optimized conditions. In contrast, photocatalysis remains underutilized in real wastewater treatment scenarios, with most studies limited to suspension-based systems tested in model solutions [48]. While these studies highlight advances in material development, their applicability is constrained by the absence of dynamic flow conditions and the complexity of real wastewater matrices, including organic matter, suspended solids, and competing species. These factors hinder the scalability of conventional photocatalytic setups and limit their adoption in municipal or hospital treatment plants.

Although some photocatalytic studies report NPX removal efficiencies exceeding 70–90 %, these results are typically obtained in batch-mode reactors operating under simplified laboratory conditions. In most cases, photocatalysts are suspended in ultrapure water spiked with NPX, irradiated using high-intensity UV sources, and tested without the presence of matrix constituents such as natural organic matter, background pharmaceuticals, or ionic species. Such conditions limit the transferability of the findings to real-world applications. In contrast, the present study demonstrates stable NPX removal (~60 %) in a modular, flow-through photocatalytic system using visible-light LED illumination across three environmentally relevant matrices: municipal tap water, secondary-treated municipal wastewater, and untreated hospital effluent. These matrices vary significantly in chemical oxygen demand, turbidity, and pharmaceutical background. Furthermore, unlike many earlier studies, the system operates with an immobilized photocatalyst and has been validated over multiple cycles without loss of performance. This configuration, supported by real-time adaptive lighting, addresses key limitations of previous approaches and highlights the potential for practical implementation in early-stage pharmaceutical load reduction.

3.6. Post-reaction surface characterization and stability of the photocatalysts

XPS analysis and FTIR spectroscopy were performed to investigate changes in the surface properties of TiO_2-Luffa and TiO_2-Sponge photocatalysts before and after NPX degradation and the adsorption of degradation by-products. Additionally, XRD analysis, SEM imaging, and EDX elemental mapping were carried out to examine structural and morphological stability after photocatalytic application. Assessing the physicochemical changes in the materials after photocatalytic treatment is essential for determining their long-term reusability and efficiency.

XPS analysis (Fig. 11a) provides an overview of the surface composition of the photocatalysts without a detailed deconvolution of specific elemental regions. The spectra show no substantial differences before and after photocatalytic degradation, indicating that the chemical structure of the materials remained largely unchanged throughout the process. However, for the TiO_2-Luffa photocatalyst, a slight but discernible increase in intensity is observed in the binding energy range around 285–288 eV, corresponding to the C 1 s region [50]. This subtle change suggests a minor accumulation of carbonaceous species, potentially indicating weak adsorption of NPX or its degradation intermediates onto the photocatalyst surface. In contrast, no significant

Table 1
Summary of literature data of NPX elimination.

Sample	Type of sewage	Type of the process	NPX concentration	Degradation efficiency (%)	Process data	Ref.
TiO_2-Luffa	Municipal	Photocatalysis	20 mg L^{-1}	60	five-step cascade; LED-IoT flow reactor; 360 min irradiation time	This work
GO-MNPs-SiO_2	Municipal	Adsorption	50 mg L^{-1}	85	batch adsorption process; adsorbent mass 60 mg; contact time 60 min	[46]
Fe-doped TiO_2 nanostructure	Synthetic	Photocatalysis	10 mg L^{-1}	90	UV–visible lamp (250 W); catalyst dosage 1.5 g L^{-1}	[47]
Pilot wastewater treatment plant	Municipal	Biodegradation (activated sludge process)	Reactor 1: 0.05 mg L^{-1} Reactor 2: 0.005 mg L^{-1}	Reactor 1: 93 % Reactor 2: 86 %	hydraulic retention time 48 h; temperature: ~22 °C (±5 %); pH: Influent ~7.7 (±2 %), effluent ~7.3 (±5 %).	[48]
Activated carbon/ alginate	Synthetic	Adsorption	50 mg L^{-1}	98 %	batch adsorption process; adsorbent mass 350 mg; contact time 360 min; pH 5.0	[49]

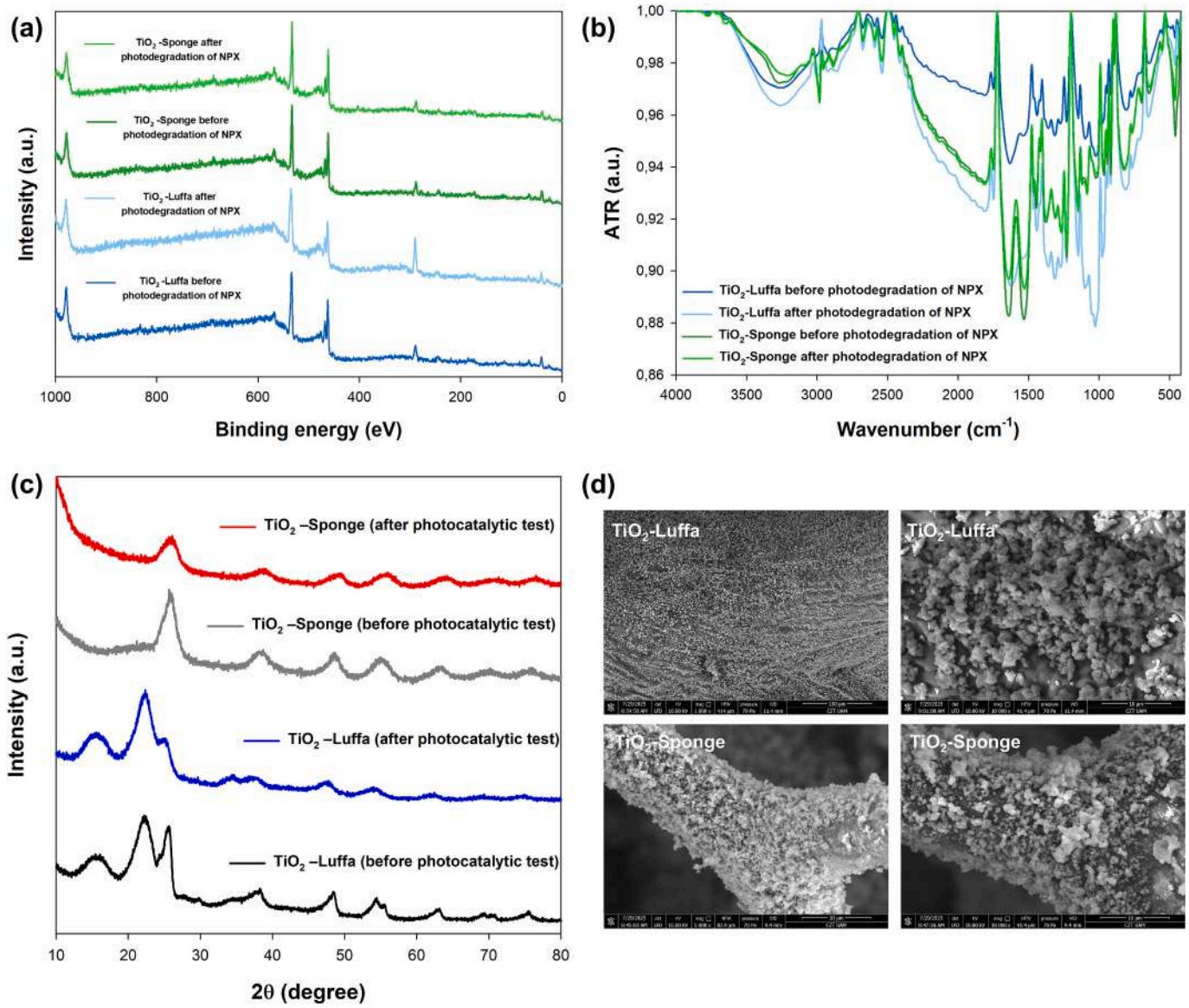

Fig. 11. (a) XPS spectra, (b) FTIR spectra, (c) XRD patterns, and (d) SEM images for photocatalysts after NPX photooxidation.

changes were observed for the TiO_2-Sponge photocatalyst, reinforcing its low tendency for contaminant adsorption.

The ATR-FTIR spectra (Fig. 11b) further support these observations. The comparison of spectra before and after NPX degradation reveals no additional functional groups that would indicate the presence of residual organic compounds on the photocatalyst surface. The dominant spectral features are primarily associated with vibrations originating from the biomimetic matrix in the 1000–1600 cm^{-1} range, which remain consistent after the photocatalytic reaction [51]. This suggests that the structural integrity of the supporting material was preserved. As

emphasized by Jensen et al. [52], ATR-FTIR spectroscopy should not be interpreted quantitatively based on signal intensity; however, the overall spectral similarity before and after photocatalysis suggests that adsorption played an insignificant role in the removal process.

The post-photocatalytic characterization was further supported by XRD analysis (Fig. 11c), SEM imaging (Fig. 11d), and EDX elemental mapping (Fig. S9, SI). The XRD patterns of the TiO_2-Luffa and TiO_2-Sponge composites before and after photocatalytic degradation revealed no detectable changes in crystallographic structure, indicating the preservation of the anatase phase and overall crystallinity. Similarly, SEM micrographs acquired after repeated photocatalytic cycles showed no signs of morphological degradation, surface delamination, or particle detachment. The EDX elemental maps confirmed the homogeneous distribution of titanium, oxygen, and carbon across the bioinspired scaffolds, consistent with the fresh materials.

These findings confirm that both TiO_2-Luffa and TiO_2-Sponge photocatalysts maintained their structural and chemical integrity following the photodegradation of NPX. The minimal changes observed in XPS and ATR-FTIR spectra suggest that adsorption played a negligible role in the removal process, with degradation occurring primarily through photocatalytic pathways. This conclusion is further supported by XRD, SEM, and EDX analyses, which revealed no observable changes in phase composition, surface morphology, or elemental distribution after photocatalytic use. Altogether, the results validate the long-term stability and reusability of these materials for wastewater treatment applications.

4. Conclusions

This study presents the development of a flow-through LED-IoT photocatalytic system integrated with bioinspired TiO_2 scaffolds for efficient degradation of pharmaceuticals, exemplified by NPX, from wastewater under variable environmental conditions. The tailored light delivery system combines solar light irradiation with artificial LED irradiation using an IoT system which autonomously regulated LED activation based on fluctuating light levels, ensuring continuous stable operation and adaptability in real-world applications.

Material characterization confirmed the uniform coating and strong adhesion of TiO_2 to the biomimetic matrices, with TiO_2-Luffa outperforming TiO_2-Sponge as results of its open structure and less dense surface favoring light penetration and water flow. Consistent photocatalytic activation and NPX degradation was achieved in field tests conducted in regions with radically different solar irradiation conditions in northern and south Europe and in different seasons. Further validation using real water matrices showed high performance in tap water (~90 %), moderate removal in municipal wastewater (~60 %), and reduced efficiency in hospital effluent (~40 %) due to matrix complexity.

This work presents a novel flow-through LED-IoT photocatalytic system specifically designed to address the persistent challenge of pharmaceutical contamination in wastewater. By offering a scalable and energy-efficient alternative to conventional treatment methods, this approach represents a significant advancement toward more resilient and sustainable water purification technologies.

CRediT authorship contribution statement

Adam Kubiak: Writing – review & editing, Writing – original draft, Visualization, Validation, Resources, Methodology, Investigation, Funding acquisition, Formal analysis, Data curation, Conceptualization. **Serena Lima:** Writing – review & editing, Validation, Resources, Data curation. **Gianluca Li Puma:** Writing – review & editing, Visualization, Validation, Supervision, Resources, Methodology, Investigation, Formal analysis, Conceptualization.

Declaration of competing interest

The authors declare the following financial interests/personal relationships which may be considered as potential competing interests: Adam Kubiak reports financial support, including travel, provided by the Initiative of Excellence – Research University (IDUB) program at Adam Mickiewicz University (Poland). Given his (Gianluca LI PUMA) role as Guest Editor in Chemical Engineering Journal, had no involvement in the peer review of this articled and had no access to information regarding its peer review. Full responsibility for the editorial process for this article was delegated to another journal editor. If there are other authors, they declare that they have no known competing financial interests or personal relationships that could have appeared to influence the work reported in this paper.

Acknowledgments

This work was supported by the National Science Centre, Poland, under grant number 2023/51/D/ST8/00206. We extend our sincere appreciation to MPECWiK Sp. z o.o., for providing us with the opportunity to conduct real-world testing of the designed photocatalytic installation. We gratefully acknowledge Lena Lighting S.A. for their support in designing the LED-IoT system, which significantly contributed to the development of our photocatalytic installation. The Department of Engineering of the University of Palermo is gratefully acknowledged for hosting Dr. Kubiak in the Environmental Nanocatalysis & Photoreaction Engineering laboratory.

Appendix A. Supplementary data

Supplementary data to this article can be found online at https://doi.org/10.1016/j.cej.2025.167518.

Data availability

Data will be made available on request.

References

[1] S. Schwarz, D. Gildemeister, A. Hein, P. Schröder, J. Bachmann, Environmental fate and effects assessment of human pharmaceuticals: lessons learnt from regulatory data, Environ. Sci. Eur. 33 (2021) 68, https://doi.org/10.1186/s12302-021-00503-0.
[2] M. Miettinen, S.A. Khan, Pharmaceutical pollution: a weakly regulated global environmental risk, Rev. Eur. Comp. Int. Environ. Law 31 (2022) 75–88, https://doi.org/10.1111/reel.12422.
[3] M. Caban, P. Stepnowski, How to decrease pharmaceuticals in the environment? A review, Environ. Chem. Lett. 19 (2021) 3115–3138, https://doi.org/10.1007/s10311-021-01194-y.
[4] S.A. Strathdee, S.C. Davies, J.R. Marcelin, Confronting antimicrobial resistance beyond the COVID-19 pandemic and the 2020 US election, Lancet 396 (2020) 1050–1053, https://doi.org/10.1016/S0140-6736(20)32063-8.
[5] European Commission, A European One Health Action Plan against Antimicrobial Resistance (AMR), June 2017.
[6] N.A. Khan, V. Vambol, S. Vambol, B. Bolibrukh, M. Sillanpaa, F. Changani, A. Esrafili, M. Yousefi, Hospital effluent guidelines and legislation scenario around the globe: a critical review, J. Environ. Chem. Eng. 9 (2021) 105874, https://doi.org/10.1016/j.jece.2021.105874.
[7] D. Su, W. Ben, B.W. Strobel, Z. Qiang, Impacts of wastewater treatment plant upgrades on the distribution and risks of pharmaceuticals in receiving rivers, J. Hazard. Mater. 406 (2021) 124331, https://doi.org/10.1016/j.jhazmat.2020.124331.
[8] M. Stec, A. Astel, Occurrence and toxicological assessment of six non–steroidal anti–inflammatory drugs (NSAIDs) in a wastewater treatment plant in Słupsk (Poland), Ecohydrol. Hydrobiol. 24 (2024) 523–534, https://doi.org/10.1016/J.ECOHYD.2024.04.007.
[9] J. Lin, Y. Zhang, Y. Bian, Y. Zhang, R. Du, M. Li, Y. Tan, X. Feng, Non-steroidal anti-inflammatory drugs (NSAIDs) in the environment: recent updates on the occurrence, fate, hazards and removal technologies, Sci. Total Environ. 904 (2023) 166897, https://doi.org/10.1016/j.scitotenv.2023.166897.
[10] Z. Mohd Hanafiah, W.H.M. Wan Mohtar, T.S.B. Abd Manan, N.A. Bachi', N. A. Abdullah, H.H. Abd Hamid, S. Beddu, N.L. Mohd Kamal, A. Ahmad, N. Wan Rasdi, The occurrence of non-steroidal anti-inflammatory drugs (NSAIDs) in

Malaysian urban domestic wastewater, Chemosphere 287 (2022) 132134, https://doi.org/10.1016/j.chemosphere.2021.132134.
[11] S. Malato, M.I. Maldonado, P. Fernández-Ibáñez, I. Oller, I. Polo, R. Sánchez-Moreno, Decontamination and disinfection of water by solar photocatalysis: the pilot plants of the Plataforma Solar de Almeria, Mater. Sci. Semicond. Process. 42 (2016) 15–23, https://doi.org/10.1016/j.mssp.2015.07.017.
[12] S.K. Loeb, P.J.J. Alvarez, J.A. Brame, E.L. Cates, W. Choi, J. Crittenden, D. D. Dionysiou, Q. Li, G. Li-Puma, X. Quan, D.L. Sedlak, T.D. Waite, P. Westerhoff, J. H. Kim, The technology horizon for photocatalytic water treatment: sunrise or sunset? Environ. Sci. Technol. 53 (2019) 2937–2947, https://doi.org/10.1021/acs.est.8b05041.
[13] E.L. Cates, Photocatalytic water treatment: so where are we going with this? Environ. Sci. Technol. 51 (2017) 757–758, https://doi.org/10.1021/acs.est.6b06035.
[14] N.S. Ali, K.R. Kalash, A.N. Ahmed, T.M. Albayati, Performance of a solar photocatalysis reactor as pretreatment for wastewater via UV, UV/TiO_2, and UV/H_2O_2 to control membrane fouling, Sci. Rep. 12 (2022) 16782, https://doi.org/10.1038/s41598-022-20984-0.
[15] D. Wang, M.A. Mueses, J.A.C. Márquez, F. Machuca-Martínez, I. Grčić, R.P. M. Moreira, G. Li Puma, Engineering and modeling perspectives on photocatalytic reactors for water treatment, Water Res. 202 (2021) 117421, https://doi.org/10.1016/j.watres.2021.117421.
[16] J.S. Roy, Y. Messaddeq, The role of solar concentrators in photocatalytic wastewater treatment, Energies 17 (2024) 4001, https://doi.org/10.3390/en17164001.
[17] M. Kositzi, I. Poulios, S. Malato, J. Caceres, A. Campos, Solar photocatalytic treatment of synthetic municipal wastewater, Water Res. 38 (2004) 1147–1154, https://doi.org/10.1016/j.watres.2003.11.024.
[18] A. Kubiak, H. Fuks, A. Szymczyk, M. Frankowski, M. Cegłowski, Development of a novel LED-IoT photoreactor for enhanced removal of carbamazepine waste driven by solar energy, J. Environ. Manag. 362 (2024) 121331, https://doi.org/10.1016/j.jenvman.2024.121331.
[19] M.B. Martinez-Pavetti, L. Medina, M. Espínola, M. Monteiro, Study on two eco-friendly surface treatments on Luffa cylindrica for development of reinforcement and processing materials, J. Mater. Res. Technol. 14 (2021) 2420–2427, https://doi.org/10.1016/j.jmrt.2021.07.141.
[20] V.H.T. Tran, B.K. Lee, Novel fabrication of a robust superhydrophobic PU@ZnO@Fe_3O_4@SA sponge and its application in oil-water separations, Sci. Rep. 7 (2017) 17520, https://doi.org/10.1038/s41598-017-17761-9.
[21] S. Zóltowska, J.F. Miñambres, A. Piasecki, F. Mertens, T. Jesionowski, Three-dimensional commercial-sponge-derived Co_3O_4@C catalysts for effective treatments of organic contaminants, J. Environ. Chem. Eng. 9 (2021) 105631, https://doi.org/10.1016/J.JECE.2021.105631.
[22] T. Jesionowski, M. Norman, S. Zółtowska-Aksamitowska, I. Petrenko, Y. Joseph, H. Ehrlich, Marine spongin: naturally prefabricated 3D scaffold-based biomaterial, Mar. Drugs 16 (2018) 88, https://doi.org/10.3390/MD16030088.
[23] S. Żółtowska, M. Modelska, A. Piasecki, T. Jesionowski, Commercial sponges in heterogeneous catalysis: developing novel composites with cobalt and silver, Physicochem. Probl. Miner. Process. 56 (2020) 89–100, https://doi.org/10.37190/ppmp/126866.
[24] M. Wysokowski, V.V. Bazhenov, M.V. Tsurkan, R. Galli, A.L. Stelling, H. Stöcker, S. Kaiser, E. Niederschlag, G. Gärtner, T. Behm, M. Ilan, A.Y. Petrenko, T. Jesionowski, H. Ehrlich, Isolation and identification of chitin in three-dimensional skeleton of Aplysina fistularis marine sponge, Int. J. Biol. Macromol. 62 (2013) 94–100, https://doi.org/10.1016/J.IJBIOMAC.2013.08.039.
[25] O.V. Petrova, D.V. Sivkov, S.V. Nekipelov, A.S. Vinogradov, P.M. Korusenko, S. I. Isaenko, R.N. Skandakov, K.A. Bakina, V.N. Sivkov, Study of marine sponges graphitization during heat treatment up to 1200 °C, Appl. Sci. 13 (2023) 128, https://doi.org/10.3390/app13010128.
[26] I. Liatsou, I. Pashalidis, M. Oezaslan, C. Dosche, Surface characterization of oxidized biochar fibers derived from Luffa cylindrica and lanthanide binding, J. Environ. Chem. Eng. 5 (2017) 4069–4074, https://doi.org/10.1016/j.jece.2017.07.040.
[27] H. Yang, X. Guo, R. Chen, Q. Liu, J. Liu, J. Yu, C. Lin, J. Wang, M. Zhang, A hybrid sponge with guanidine and phytic acid enriched surface for integration of antibiofouling and uranium uptake from seawater, Appl. Surf. Sci. 525 (2020) 146611, https://doi.org/10.1016/J.APSUSC.2020.146611.
[28] M. Chi, X. Sun, G. Lozano-Blanco, B.J. Tatarchuk, XPS and FTIR investigations of the transient photocatalytic decomposition of surface carbon contaminants from anatase TiO_2 in UHV starved water/oxygen environments, Appl. Surf. Sci. 570 (2021) 151147, https://doi.org/10.1016/j.apsusc.2021.151147.
[29] B. Erdem, R.A. Hunsicker, G.W. Simmons, E.D. Sudol, V.L. Dimonie, M.S. El-Aasser, XPS and FTIR surface characterization of TiO_2 particles used in polymer encapsulation, Langmuir 17 (2001) 2664–2669, https://doi.org/10.1021/la0015213.
[30] J. Yang, H. Bai, X. Tan, J. Lian, IR and XPS investigation of visible-light photocatalysis: nitrogen-carbon-doped TiO_2 film, Appl. Surf. Sci. 253 (2006) 1988–1994, https://doi.org/10.1016/j.apsusc.2006.03.078.
[31] Y. Park, W. Kim, H. Park, T. Tachikawa, T. Majima, W. Choi, Carbon-doped TiO_2 photocatalyst synthesized without using an external carbon precursor and the visible light activity, Appl Catal B 91 (2009) 355–361, https://doi.org/10.1016/j.apcatb.2009.06.001.
[32] A. Kubiak, A. Grzegórska, E. Gabała, J. Zembrzuska, M. Szybowicz, H. Fuks, A. Szymczyk, A. Zielińska-Jurek, M. Sikorski, T. Jesionowski, TiO_2–C nanocomposite synthesized via facile surfactant-assisted method as a part of less energy-consuming LED-based photocatalytic system for environmental applications, J. Photochem. Photobiol. A Chem. 437 (2023) 114428, https://doi.org/10.1016/j.jphotochem.2022.114428.
[33] Y.W. Chen, Y.H. Hsu, Effects of reaction temperature on the photocatalytic activity of TiO_2 with Pd and cu cocatalysts, Catalysts 11 (2021) 966, https://doi.org/10.3390/catal11080966.
[34] S. Corbel, N. Becheikh, T. Roques-Carmes, O. Zahraa, Mass transfer measurements and modeling in a microchannel photocatalytic reactor, Chem. Eng. Res. Des. 92 (2014) 657–662, https://doi.org/10.1016/J.CHERD.2013.10.011.
[35] M. Malayeri, C.S. Lee, F. Haghighat, L. Klimes, Modeling of gas-phase heterogeneous photocatalytic oxidation reactor in the presence of mass transfer limitation and axial dispersion, Chem. Eng. J. 386 (2020) 124013, https://doi.org/10.1016/J.CEJ.2020.124013.
[36] H. Amiri, B. Ayati, H. Ganjidoust, Mass transfer phenomenon in photocatalytic cascade disc reactor: effects of artificial roughness and flow rate, Chem. Eng. Process. 116 (2017) 48–59, https://doi.org/10.1016/J.CEP.2017.03.004.
[37] S. Sharma, R.K. Yadav, A.P. Singh, Presence of medicinal materials in drinking water: a review, Mater Today Proc 61 (2022) 1067–1072, https://doi.org/10.1016/j.matpr.2021.10.336.
[38] J.A. Rodrigues, S. Silva, V.V. Cardoso, M.J. Benoliel, E. Cardoso, M.R. Coelho, A. Martins, C.M.M. Almeida, Screening and seasonal behavior of analgesics, non-steroidal anti-inflammatory drugs, and antibiotics in two urban wastewater treatment plants, Environ. Manag. 68 (2021) 411–425, https://doi.org/10.1007/s00267-021-01496-5.
[39] A. Eslami, M.M. Amini, A.R. Yazdanbakhsh, N. Rastkari, A. Mohseni-Bandpei, S. Nasseri, E. Piroti, A. Asadi, Occurrence of non-steroidal anti-inflammatory drugs in Tehran source water, municipal and hospital wastewaters, and their ecotoxicological risk assessment, Environ. Monit. Assess. 187 (2015) 1–15, https://doi.org/10.1007/s10661-015-4952-1.
[40] M. Jiménez-Salcedo, M. Monge, M.T. Tena, The photocatalytic degradation of naproxen with g-C_3N_4 and visible light: identification of primary by-products and mechanism in tap water and ultrapure water, J. Environ. Chem. Eng. 10 (2022) 106964, https://doi.org/10.1016/J.JECE.2021.106964.
[41] G. Fan, R. Ning, J. Luo, J. Zhang, P. Hua, Y. Guo, Z. Li, Visible-light-driven photocatalytic degradation of naproxen by Bi-modified titanate nanobulks: synthesis, degradation pathway and mechanism, J. Photochem. Photobiol. A Chem. 386 (2020) 112108, https://doi.org/10.1016/J.JPHOTOCHEM.2019.112108.
[42] A. Eslami, M.M. Amini, A. Asadi, A.A. Safari, N. Daglioglu, Photocatalytic degradation of ibuprofen and naproxen in water over NS-TiO_2 coating on polycarbonate: process modeling and intermediates identification, Inorg. Chem. Commun. 115 (2020), https://doi.org/10.1016/j.inoche.2020.107888.
[43] X. Cheng, X. Yu, Z. Xing, J. Wan, Enhanced photocatalytic activity of nitrogen doped TiO_2 anatase nanoparticle under simulated sunlight irradiation, Energy Procedia (2012) 598–605, https://doi.org/10.1016/j.egypro.2012.01.096.
[44] O. Muktaridha, M. Adlim, S. Suhendrayatna, I. Ismail, Progress of 3d metal-doped zinc oxide nanoparticles and the photocatalytic properties, Arab. J. Chem. 14 (2021) 103175, https://doi.org/10.1016/j.arabjc.2021.103175.
[45] https://www.epa.gov/tsca-screening-tools/ecological-structure-activity-relationships-ecosar-predictive-model [Date of access 24 May 2025].
[46] M.K. Mohammadi Nodeh, M. Radfard, L.A. Zardari, H. Rashidi Nodeh, Enhanced removal of NPX from wastewater using silica magnetic nanoparticles decorated onto graphene oxide: parametric and equilibrium study, Sep. Sci. Technol. 53 (2018) 2476–2485, https://doi.org/10.1080/01496395.2018.1457054.
[47] M. Hinojosa–Reyes, R. Camposeco–Solis, F. Ruiz, V. Rodríguez–González, E. Moctezuma, Promotional effect of metal doping on nanostructured TiO_2 during the photocatalytic degradation of 4-chlorophenol and NPX sodium as pollutants, Mater. Sci. Semicond. Process. 100 (2019) 130–139, https://doi.org/10.1016/j.mssp.2019.04.050.
[48] T. Kosjek, E. Heath, B. Kompare, Removal of pharmaceutical residues in a pilot wastewater treatment plant, Anal. Bioanal. Chem. (2007) 1379–1387, https://doi.org/10.1007/s00216-006-0969-1.
[49] N. Ozcan, D. Saloglu, Activated carbon embedded alginate beads for removing nonsteroidal anti-inflammatory drug NPX from wastewater: equilibrium, kinetics, thermodynamics, desorption, and reusability, Water Sci. Technol. 81 (2020) 1432–1444, https://doi.org/10.2166/wst.2020.196.
[50] M. Chi, X. Sun, A. Sujan, Z. Davis, B.J. Tatarchuk, A quantitative XPS examination of UV induced surface modification of TiO_2 sorbents for the increased saturation capacity of sulfur heterocycles, Fuel 238 (2019) 454–461, https://doi.org/10.1016/j.fuel.2018.10.114.
[51] C. Parida, S.K. Dash, C. Pradhan, FTIR and raman studies of cellulose fibers of *Luffa cylindrica*, Open J. Compos. Mater. 5 (2015) 5–10, https://doi.org/10.4236/ojcm.2015.51002.
[52] E.A. Jensen, D. Smith, P. Chapela, S.M. Lederer, Caution in interpreting FTIR/ATR spectral intensity values, Analyst 142 (2017) 3797–3799, https://doi.org/10.1039/c7an00704c.